

Author(s)	Caldwell, David M
Title	Observation and analysis of optical transition radiation at the NPS linac and its use for diagnostics of electron beams
Publisher	Monterey, California. Naval Postgraduate School
Issue Date	1990
URL	http://hdl.handle.net/10945/38000

This document was downloaded on December 20, 2013 at 09:04:28



<http://www.nps.edu/library>

Calhoun is a project of the Dudley Knox Library at NPS, furthering the precepts and goals of open government and government transparency. All information contained herein has been approved for release by the NPS Public Affairs Officer.

Dudley Knox Library / Naval Postgraduate School
411 Dyer Road / 1 University Circle
Monterey, California USA 93943



<http://www.nps.edu/>

NPS ARCHIVE
1990.06
CALDWELL, D.

NAVAL POSTGRADUATE SCHOOL Monterey, California



THESIS

OBSERVATION AND ANALYSIS OF
OPTICAL TRANSITION RADIATION AT THE NPS LINAC
AND ITS USE FOR DIAGNOSTICS OF ELECTRON BEAMS

by

David Matthew Caldwell

June 1990

Thesis Advisor

X.K. Maruyama

Approved for public release; distribution is unlimited

DUDLEY KNOX LIBRARY
NAVAL POSTGRADUATE SCHOOL
MONTEREY, CALIFORNIA 93943-8002

REPORT DOCUMENTATION PAGE				Form Approved OMB No 0704-0188	
1a REPORT SECURITY CLASSIFICATION Unclassified			1b RESTRICTIVE MARKINGS		
2a SECURITY CLASSIFICATION AUTHORITY			3 DISTRIBUTION/AVAILABILITY OF REPORT Approved for public release; distribution is unlimited		
2b DECLASSIFICATION/DOWNGRADING SCHEDULE					
4 PERFORMING ORGANIZATION REPORT NUMBER(S)			5 MONITORING ORGANIZATION REPORT NUMBER(S)		
6a NAME OF PERFORMING ORGANIZATION Naval Postgraduate School		6b OFFICE SYMBOL (If applicable) 33	7a NAME OF MONITORING ORGANIZATION Naval Postgraduate School		
6c ADDRESS (City, State, and ZIP Code) Monterey, CA 93943-5000			7b ADDRESS (City, State, and ZIP Code) Monterey, CA 93943-5000		
8a NAME OF FUNDING SPONSORING ORGANIZATION		8b OFFICE SYMBOL (If applicable)	9 PROCUREMENT INSTRUMENT IDENTIFICATION NUMBER		
8c ADDRESS (City, State, and ZIP Code)			10 SOURCE OF FUNDING NUMBERS		
			PROGRAM ELEMENT NO	PROJECT NO	TASK NO
					WORK UNIT ACCESSION NO
11 TITLE (Include Security Classification) OBSERVATION AND ANALYSIS OF OPTICAL TRANSITION RADIATION AT THE NPS LINAC AND ITS USE FOR DIAGNOSTICS FOR ELECTRON BEAMS					
12 PERSONAL AUTHOR(S) Caldwell, David, Matthew					
13a TYPE OF REPORT Master's Thesis		13b TIME COVERED FROM _____ TO _____		14 DATE OF REPORT (Year, Month, Day) 1990, June	
15 PAGE COUNT 81					
16 SUPPLEMENTARY NOTATION The views expressed in this thesis are those of the author and do not reflect the official policy or position of the Department of Defense or the U.S. Government					
17 COSATI CODES			18 SUBJECT TERMS (Continue on reverse if necessary and identify by block number)		
FIELD	GROUP	SUB-GROUP	Transition Radiation, Diffraction pattern, Lorentz Factor, Electron beam current, Integrated Density		
19 ABSTRACT (Continue on reverse if necessary and identify by block number) An experimental technique for observing Optical Transition Radiation, (OTR), that is both simple and effective, is shown. A Macintosh II computer equipped with an image frame grabber board and <i>Image</i> software package allows for extensive analysis of the captured electron beam spot OTR patterns. The equipment is capable of measuring relative intensities to better than 1% for a constant source image. With beam energies of nearly 100 MeV the captured OTR images show an unexpected asymmetry in the beam intensity profile. The variations of the beam intensity and shape are shown for nominally steady beam conditions. Using <i>Image</i>, integrated signals of the beam spot OTR patterns for several targets as a function of beam current show a linear relationship, thereby creating a technique for computing electron beam current. Portions of the beam profile with varying percentages of beam spot maximum intensity also show a linear relationship between beam current and OTR image intensity. A radiation cone OTR pattern has been observed for the NPS linac beam. From the pattern, the Lorentz factor for the 100 MeV electrons is observed to be less than the computed value, and probably indicates the non-collinearity of the electron beam.					
20 DISTRIBUTION/AVAILABILITY OF ABSTRACT <input checked="" type="checkbox"/> UNCLASSIFIED/UNLIMITED <input type="checkbox"/> SAME AS RPT <input type="checkbox"/> DTIC USERS			21 ABSTRACT SECURITY CLASSIFICATION Unclassified		
22a NAME OF RESPONSIBLE INDIVIDUAL Prof. Xavier K. Maruyama			22b TELEPHONE (Include Area Code) (408) 646-2431		22c OFFICE SYMBOL 61Mx

Approved for public release; distribution is unlimited

Observation and Analysis of Optical Transition Radiation at the NPS Linac
and its Use for Diagnostics of Electron Beams

by

David M. Caldwell
Lieutenant, United States Navy
B.S., United States Naval Academy, 1984

Submitted in partial fulfillment of the
requirements for the degree of

MASTER OF SCIENCE IN PHYSICS


from the


NAVAL POSTGRADUATE SCHOOL
June 1990


Author:


David M. Caldwell

Approved by:


Xavier K. Maruyama, Thesis Advisor


John R. Neighours, Second Reader


Karlheinz E. Woehler, Chairman,
Department of Physics

ABSTRACT

An experimental technique for observing Optical Transition Radiation, (OTR), that is both simple and effective, is shown. A Macintosh II computer equipped with an image frame grabber board and *Image* software package allows for extensive analysis of the captured electron beam spot OTR patterns. The equipment is capable of measuring relative intensities to better than 1% for a constant source image. With beam energies of nearly 100 MeV the captured OTR images show an unexpected assymetry in the beam intensity profile. The variations of the beam intensity and shape are shown for nominally steady beam conditions. Using *Image*, integrated signals of the beam spot OTR patterns for several targets as a function of beam current show a linear relationship, thereby creating a technique for computing electron beam current. Portions of the beam profile with varying percentages of beam spot maximum intensity also show a linear relationship between beam current and OTR image intensity. A radiation cone OTR pattern has been observed for the NPS linac beam. From the pattern, the Lorentz factor for the 100 MeV electrons is observed to be less than the computed value, and probably indicates the non-collinearity of the electron beam.

NPS ARCHIVE
1990.06
CALDWELL, D.

~~Thesis~~
~~C186273~~
~~C.2~~

TABLE OF CONTENTS

I.	INTRODUCTION	1
	A. THEORY OF OPTICAL TRANSITION RADIATION	1
	B. PREVIOUS OTR WORK AT NPS	5
	C. PURPOSE OF EXPERIMENT	6
II.	THE EXPERIMENT	7
	A. EXPERIMENTAL SETUP	7
	1. The Control Room	7
	2. Target Area	7
	B. EXPERIMENTAL PROCEDURE	10
	1. Alignment	10
	2. Focusing Requirements	13
III.	PRELIMINARY CONSIDERATIONS	16
	A. COMPUTER SOFTWARE	16
	B. EQUIPMENT CAPABILITIES	27
	1. A Constant Light Source	27
	2. Camera Response	28
IV.	EXPERIMENTAL RESULTS	30
	A. RESULTS	30
	B. CONCLUSIONS	66
	C. RECOMMENDATIONS	68

APPENDIX A LIST OF EQUIPMENT	70
LIST OF REFERENCES	72
INITIAL DISTRIBUTION LIST	73

Acknowledgements

I'd like to thank Professor Xavier Maruyama for his guidance and support during the writing of this thesis. My limited understanding of the subject matter was greatly increased through his conscientious efforts.

Professor Fred Buskirk deserves special recognition as a "highly paid consultant." Not only did he provide for several hours of electron beam time, but he also advised me on experimental techniques and data analysis methods.

Without properly working equipment, this work would not have been possible. For their efforts in reestablishing a working accelerator after the Loma Prieta earthquake and insuring that all associated gear was functioning properly, Mr. Don Snyder and Mr. Harold Reitdyk are thanked immensely.

Most importantly, I'd like to thank my wife [REDACTED] for her patience and support in allowing for the successful completion of this work. Her ability to manage a household without my assistance is proof of her strong will and respect for the importance of my education. Her efforts were not unnoticed, and they will certainly be repaid. I dedicate this work to her.

I. INTRODUCTION

A. THEORY OF OPTICAL TRANSITION RADIATION

The concept of Cerenkov radiation, that is the radiation caused by a charged particle moving in a medium at a speed faster than the speed of light in that same medium, had been known since about 1939. It wasn't until 1944 that the concept of transition radiation was presented. Ginsburg and Frank [Ref. 1] first theorized that a charged particle which experiences a change in the dielectric properties of the medium through which it travels produces electromagnetic radiation. This radiation became known as transition radiation, and manifests itself in the form of photons which cover a wide frequency spectrum depending on the energy of the charged particle causing the radiation. The radiation of photons which have frequencies in the optical region is known as optical transition radiation, OTR, and is the subject of this paper.

In their paper [Ref. 1] Ginsburg and Frank developed rigorous mathematical formulas which describe the physics governing transition radiation for a charged particle transiting a boundary between two dielectrically different media [Ref. 2]. Although the derivation of those equations here would be beyond the scope of this paper, a brief explanation of the physics involved will be given, and the equation relating radiation intensity and observation angle will be presented. Probably the most effective and certainly the simplest description of transition radiation uses the concept of image charges as is often used in the understanding of electromagnetic fields from a point charge near a conducting boundary [Ref. 3]. In this model, a single particle

of charge q approaches the boundary between two media at the same rate that its "image" particle of charge $-q$ approaches from the opposite direction. Figure 1 illustrates the model.

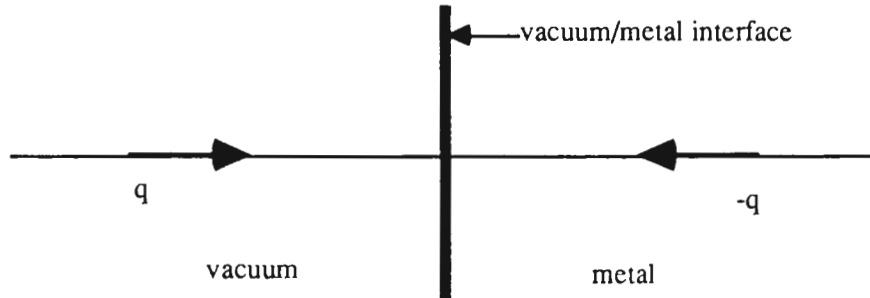


Figure 1: Model of particle and its image particle approaching a vacuum/metal interface thereby acting as a collapsing dipole and producing transition radiation [Ref. 3].

At the instant the two particles meet, radiation fields must necessarily be produced to satisfy the inhomogeneous Maxwell equations, and these required radiation fields are just the transition radiation [Ref. 2]. The equations derived by Ginsburg and Frank used to describe this phenomena relate the intensity of the forward or backward scattered radiation per frequency interval per solid angle around the particle's line of motion as a function of the particle's velocity, the angle of observation and the dielectric characteristics of the two media. If the charged particle is experiencing a transition from vacuum to a perfect conductor, the equation describing the radiation intensity is

$$\frac{dI(\omega, \theta)}{d\omega d\Omega} = \frac{e^2 \beta^2 \sin^2 \theta}{\pi^2 c [1 - \beta^2 \cos^2 \theta]^2} \quad (\text{Eqn. 1}),$$

where $d\Omega$ is the solid angle about θ , the angle of observation as measured from the normal to the surface and $\beta = v/c$ with c the velocity of light [Ref. 4]. From Equation 1 it can be seen that the radiation pattern is cone shaped, and that the intensity has a strong dependence on the angle of observation. The peak intensity I_p , occurs at an angle θ_p which is inversely proportional to the ratio of the total relativistic and rest mass energies of the charged particle, commonly referred to as the Lorentz factor and given the symbol γ . Figure 2 shows an OTR intensity profile. Note that a three dimensional intensity plot would yield the characteristic donut shape of the radiation cone. In actual experiments, it is difficult to observe OTR in the forward or backward direction since the radiation cone surrounds the charged particle beam itself. Instead, if one were to orient whatever target device is used to create the transition radiation at an oblique angle to the direction of motion of the charged particles, then the backward radiation cone would be observable around the angle of specular reflection [Ref. 5]. Specifically, if one were to orient the target device so that the charged particles strike it at an angle of 45° then the backward OTR could be observed perpendicular to the beam. This is in fact the method used to observe OTR in this experiment. Figure 3 shows the optical transition radiation patterns for both normal and oblique incidence on a planar target device.

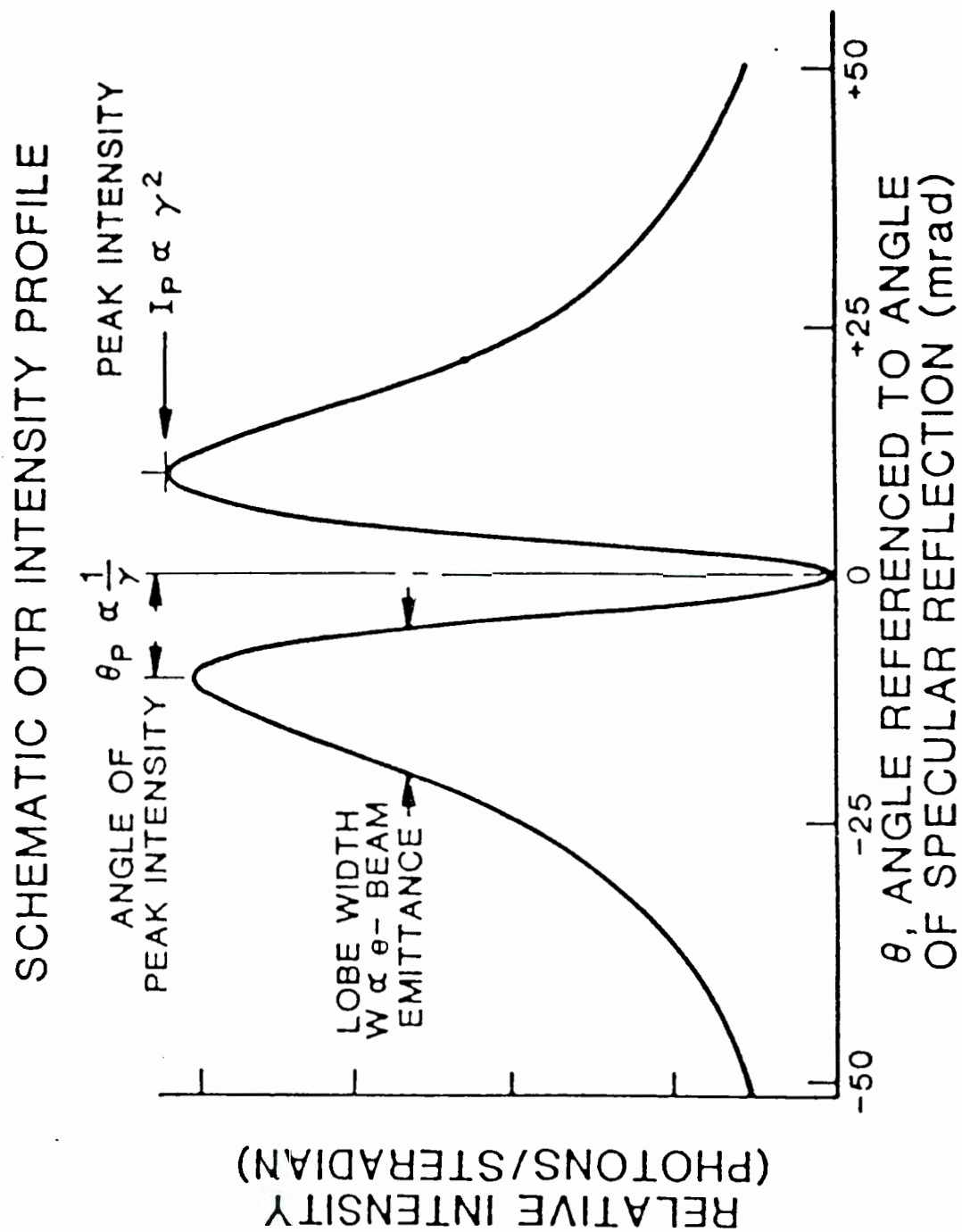


Figure 2: Schematic OTR Intensity profile. The angle of peak intensity is inversely proportional to γ , the Lorentz factor [Ref. 6].

OPTICAL TRANSITION RADIATION PATTERNS

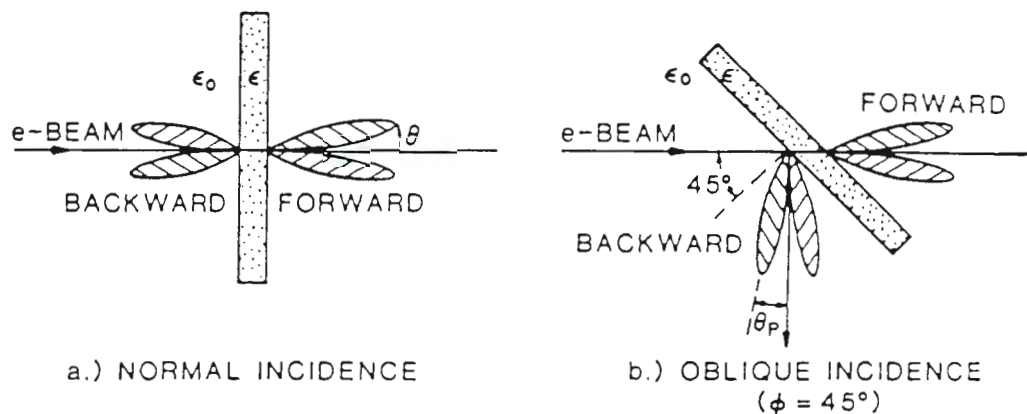


Figure 3: Optical Transition Radiation patterns caused by an electron beam striking a target at both normal and oblique incidence. Figure b depicts the experimental approach described in this paper. (Figure from Ref. 7)

B. PREVIOUS OTR WORK AT NPS

Transition radiation experiments at the NPS linear accelerator to date have been chiefly concerned with investigating the forward scattered radiation in the X-ray region. OTR observations at NPS were first made in connection with the MS Thesis of W.G. Longstaff [Ref 8]. Dallman [Ref. 9] was the first to attempt to observe OTR by using an experimental setup similar to that of Maruyama, Fiorito, and Rule [Ref. 5] in their work to apply the diagnostic capabilities of OTR to free electron laser systems. Unfortunately, equipment inoperability due to the 17 October 1989 Loma Prieta earthquake prevented Dallman from actually observing OTR except once. He did however prove the usefulness of the experimental approach and equipment for observing OTR by applying the same concepts involved to a laser beam. For example, he proved the ease with

which the microcomputer and accompanying software captured and displayed digitized images of laser beam intensity profiles, a process which is of great importance in OTR experiments. Dallman's work serves as the starting point for this experiment. In fact, with only a few minor exceptions, the experimental approach and equipment is identical to that utilized by Dallman.

C. PURPOSE OF EXPERIMENT

Dallman [Ref.9] proved the capability to observe OTR with the experimental setup described both in his work and later in this paper. It is the purpose of this experiment to utilize that capability and show that not only is the equipment effective in capturing OTR images, but also in providing useful information of the electron beam characteristics. It will be shown that the equipment and experimental technique allow one to capture OTR images of the electron beam and backward scattered radiation cone; that the microcomputer and software capture and display a real-time, three dimensional beam intensity profile which can be viewed and analyzed through 360°; and that the software allows for integration of the captured OTR image, a function which proves useful in computing electron beam current. Finally, a calculation of the Lorentz factor will be performed using experimental data.

II. THE EXPERIMENT

A. EXPERIMENTAL SETUP

1. The Control Room

Due to radiation concerns in all charged particle beam accelerator experiments, the capability to remotely operate and observe diagnostic equipment that is within the radiation area is essential. The same is true for this experiment. In the control room is a Macintosh II computer equipped with a Data Translation DT 2255 - 60 Hz Quick Capture Frame Grabber Board and accompanying software. This is the most essential piece of equipment used in obtaining and analyzing the experimental data. The computer receives as its input a video signal from one of several cameras located in the target area, each viewing the actual target device from a different angle. By using the *Image* software, a set of public domain programs provided by Wayne Rasband of the National Institutes of Health [Ref. 10] one can capture and store images for either immediate or future analysis. Also located in the control room are two remote stepping motors; one that is used for changing the orientation of several target devices with respect to the electron beam axis, and the other used for allowing one to change the point of focus of one particular camera for viewing both beam spot and radiation cone OTR.

2. Target Area

The target area, or end station is the area where electrons strike a target thereby producing OTR. The equipment arrangement is shown in Figure 4. As can be seen in that figure, an optical bench is placed immediately beside two target chambers that are in the line of the electron beam. This bench serves as a planar surface to which several optical devices may be

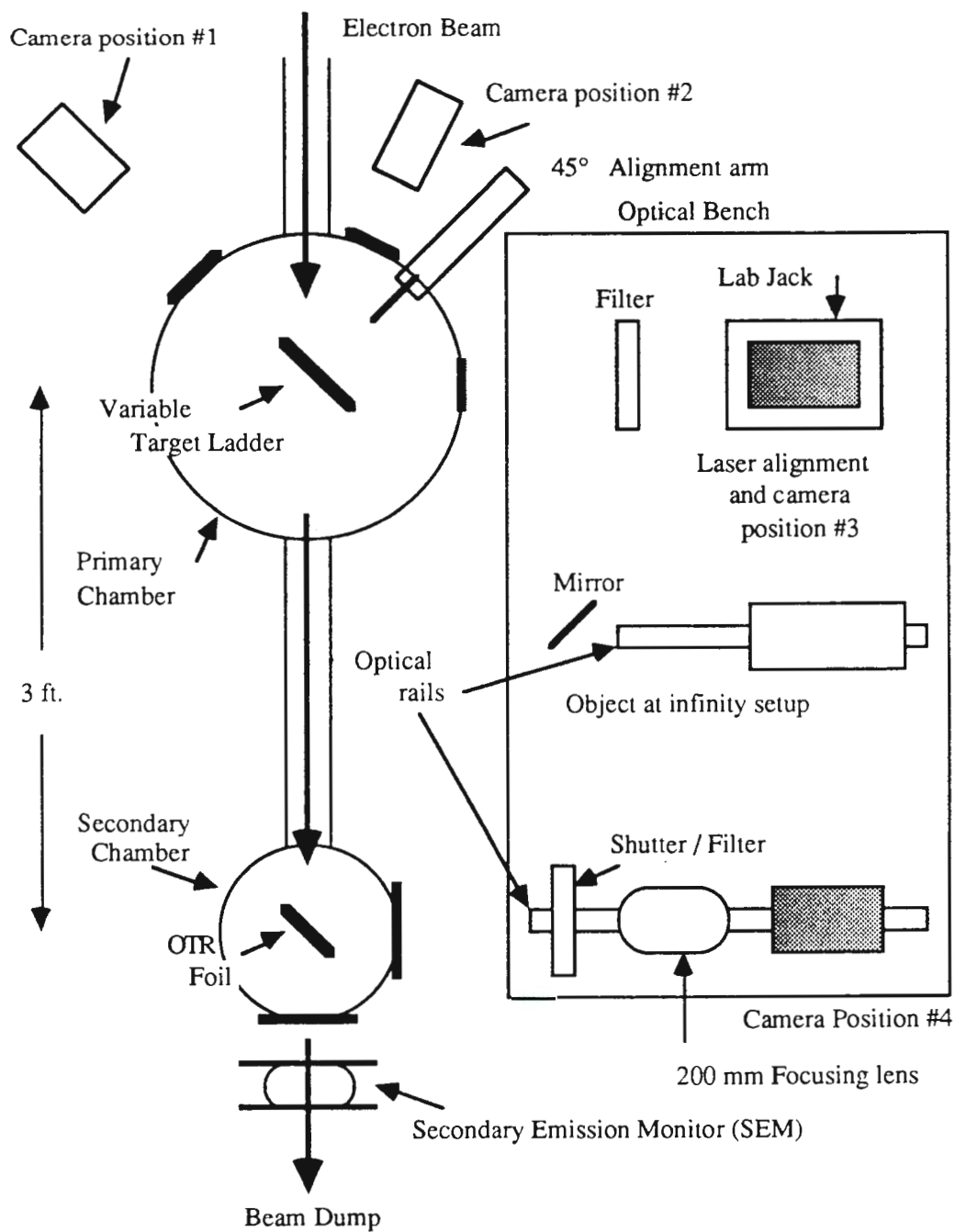


Figure 4: Target area / end station equipment setup. The placement of several cameras allows for viewing OTR from the target devices at several different angles.

placed and aligned with relative accuracy. This need for alignment accuracy will be discussed in a later section. The primary chamber has several viewports, an alignment arm, and a rotatable/variable target ladder. Three of the primary chamber viewports were used in this experiment, and are designated camera positions #1 through #3. Camera position #1 was used exclusively for steering and focusing the electron beam. Camera positions #2 and #3 were used for observing OTR. The alignment arm is used in conjunction with a laser to align a camera at position #4 for viewing OTR from the secondary chamber. The rotatable/variable target ladder allows for positioning of various targets which may be moved vertically in a plane to allow for observing OTR from different planar sources. It is also rotatable so that information concerning beam spot and radiation cone angular divergence may be obtained. Down stream of the primary chamber is a secondary chamber which houses an OTR foil.

On the optical bench are located several devices used for aligning cameras and viewing OTR. At camera position #4 is placed a COHU model number 4815/5000 low intensity light, solid state camera. This camera differs from the SITCAM used by Dallman [Ref. 9] in that it is much more compact, and it requires no separate camera control unit. Immediately in front of the COHU is a 200 mm lens whose position is remotely adjustable to allow for focusing the camera for viewing either beam spot or radiation cone OTR. Also in front of the COHU is a shutter / filter mechanism which allows one to place neutral density filters in the line of the backward OTR pattern and to protect the camera from becoming saturated with OTR light. Finally, on the optical bench is an "object at infinity" setup which allows one to place the COHU at the focal point of the 200 mm lens for viewing parallel light in the form of OTR.

Not shown in the figure is a set of focusing and steering magnets for the electron beam which are located upstream of the primary chamber. Lastly, downstream of both chambers is located a secondary emissions monitor (SEM) used for measuring beam current.

B. EXPERIMENTAL PROCEDURE

1. Alignment

As was shown in Equation 1 and Figure 2, the dependence of radiation intensity on observation angle is significant. It is for this reason that a strict alignment procedure is called for. The underlying concept, as described by Dallman [Ref. 9] is to align optical devices with a laser beam so that the laser beam is collinear with the electron beam. If this can be achieved, then observing OTR should be relatively easy provided that the beam energy is enough to produce an intense enough OTR pattern. Although the alignment procedure is tedious it allows for accuracy in insuring the collinearity of the laser and the electron beam.

Initial considerations were to insure that the optical bench, the primary and secondary chambers, and the vacuum piping connecting the chambers were all level. This was accomplished with relative ease by using a simple leveling device. Next, a laser mounted on a lab jack placed at position #3, was centered and retro-reflected off the viewport associated with that camera position. By securing the lab jack to the optical bench at this point, it remains aligned so that a camera may be placed here for future use. The 45° alignment arm with a mirror attached was then placed in the line of the laser so that it may be reflected down towards the secondary chamber. To ensure that the laser travelled down the geometric center of the vacuum piping, fiducials are placed at the exit port of the primary chamber in the direction of the

secondary chamber and at the beam dump side of the secondary chamber. The reflected laser beam is then "steered" through the two fiducials by adjusting four set screws on the 45° alignment arm which orient the mirror at the proper angle. Next, the OTR foil in the secondary chamber is placed in the line of the laser so that it reflects out of the viewport associated with camera position #4. Another fiducial is placed on this viewport and the OTR foil is oriented so that the laser passes through it. At this point in the alignment procedure, the laser beam is travelling down the center of the vacuum piping, and is exiting viewport position #4 at the same height from the optical bench as it was when it entered viewport position #3. The next step is to align the optical rail which holds the COUH camera and the 200 mm lens. It is not sufficient to simply retro-reflect the laser from the faces of the lens and the camera, because the lens is attached to a moveable track which allows for remote focusing of the camera, and will therefore require strict alignment along the entire length of the optical rail. To align the rail, one simply places any device in an optical stand which is fitted to the rail and observes the point where the laser strikes this device at the extremes of the rail. Once a point where the laser strikes the device at the same spot at both extremes is obtained, the rail is aligned. Finally, the COHU camera and the 200 mm lens are retro-reflected back onto the window in viewport #4. Centering fiducials are placed on the faces of the lens and the camera to ensure that the laser beam strikes them on their geometric centers.

The above procedure aligns the optical devices to the laser beam. It is now important to insure that the electron beam travels down the same path as the laser beam. To accomplish this, two points in space are required to insure collinearity. The first point is on the backside of the 45° alignment mirror. The actual mirror is only half silvered so that some of the laser light passes

through it. A phosphorus screen with a pin-point hole in it is placed on the backside of the mirror in such a fashion that the laser beam passes through the center of the hole. Phosphorus is used because electrons striking a surface covered with it cause it to glow. In the experimental setup of Figure 4 it can be seen that a camera placed at position #1 will allow for viewing the electron beam at this point. The second point used for coupling the laser and the electron beam is on the face of the camera itself placed at position #4. Once the above laser alignment procedure is accomplished, the camera may be turned on and an actual laser beam spot captured with the computer. With the *Image* software the position on the computer screen of the laser beam spot may be determined. If one can steer the electron beam through these two points, then collinearity of the two beams is accomplished. At first glance this procedure seems appropriate, but one can see that in order to steer the electron beam through the same point on the camera face as the laser beam, one must use the OTR from the electron beam striking the foil in the secondary chamber. This seems rather inappropriate in that the alignment procedure is designed to insure that one may observe OTR in the first place. In fact, this caused some concern prior to actually running the experiment. It was then determined that based on the known capabilities of the electron beam steering magnets, the experiment should proceed using only the one point in the primary chamber to attempt to achieve collinearity. If after steering the electron beam through that point OTR was not seen on the the foil in the secondary chamber, then the beam could be steered slightly until OTR was seen. Although this appears to be a somewhat sketchy way of approaching the problem, it was not certain at the start whether the beam steering magnets had the capability of placing the beam on the exact path of the laser. The determination of proceeding with the experiment with only the one common point of focus

therefore seems valid. The decision is even further justified by the fact that OTR was seen on at least two previous occasions with the same camera setup using only a mirror in the primary chamber and a less stringent alignment procedure.

As previously mentioned, the laser was mounted on a lab jack secured to the optical bench. The reason for insuring that the lab jack remain aligned was so that the laser could be removed and replaced by a second camera. This camera could be utilized for viewing OTR from one of several targets on the ladder mechanism in the primary chamber. This position could also be used by the COHU with the 200 mm lens to focus sharply on the same targets.

2. Focusing Requirements

Figure 4 showed an "object at infinity" arrangement. As was stated above, this setup allows one to place the COHU camera at the focal point of the 200 mm lens. The reason for doing this is that in order to observe the radiation cone OTR, the optical equipment should be aligned and focused to see parallel light. Figure 5 shows an optical ray diagram for OTR imaging. As can be seen by following the ray tracings of the OTR radiation patterns from the object plane through the lens, the double-humped OTR radiation pattern is visible at the focal point. The beam profile OTR radiation pattern is visible at the image plane. It is because of these two focusing points that the 200 mm lens is attached to a remotely controlled, motorized stage. Dallman [Ref. 9] discusses the dimensional requirements for the translational stage.

In order to focus accurately on the OTR foil itself as is required for viewing electron beam profile OTR, a small ruler was affixed to the mounting bracket holding the foil. When the camera was turned on and focused on the foil, not only was the ruler clearly visible, but so were several small scratches on the foil surface. These scratches proved to be the most effective means of remotely

OPTICAL RAY DIAGRAM FOR OTR IMAGING

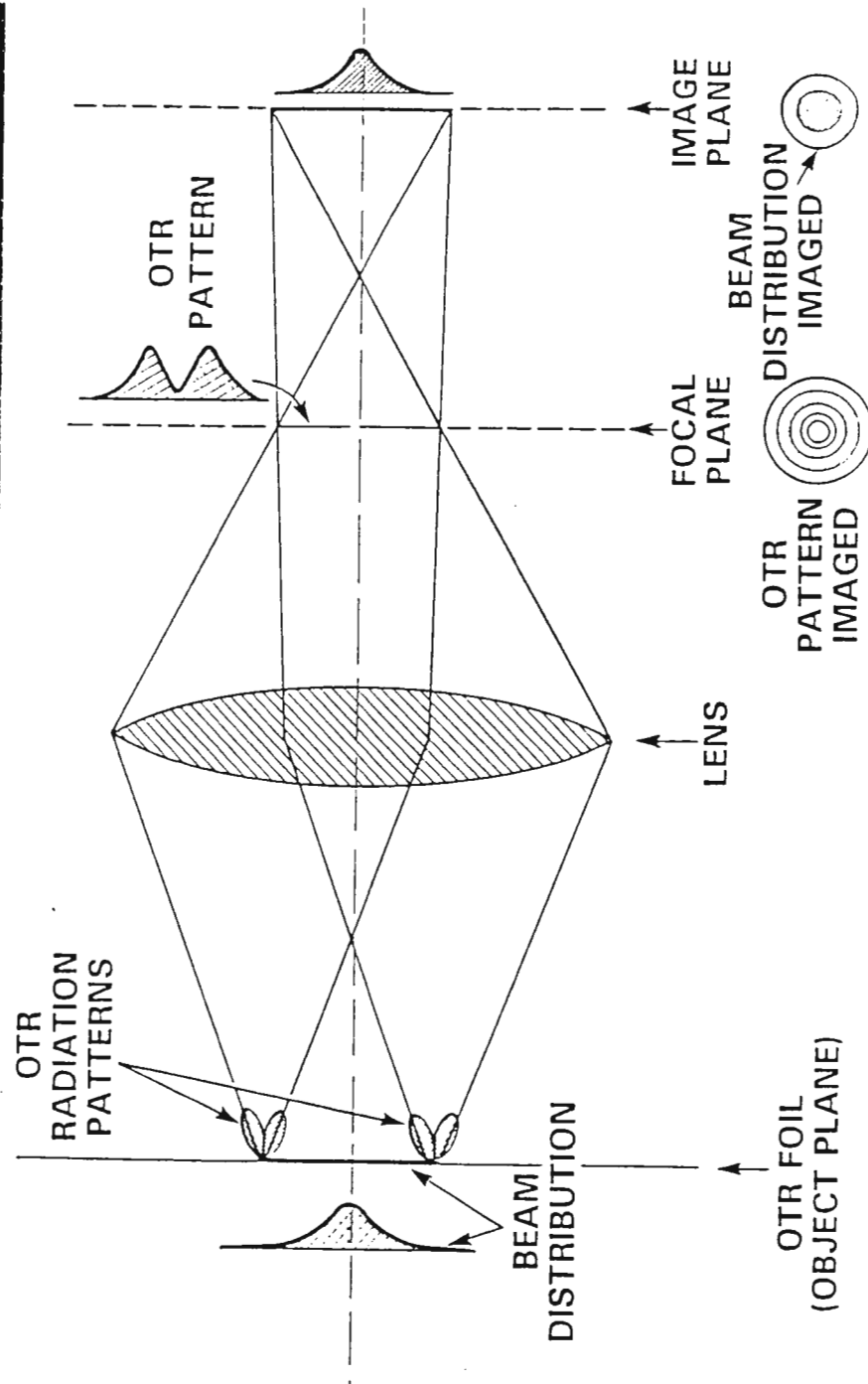


Figure 5: Optical Ray Diagram for OTR imaging. Radiation cone OTR is visible at the focal point of the lens while beam spot OTR is visible at the image plane. [Ref. 6]

focusing the camera. In order to focus the camera at infinity for viewing the radiation cone, the setup shown in Figure 6 was used.

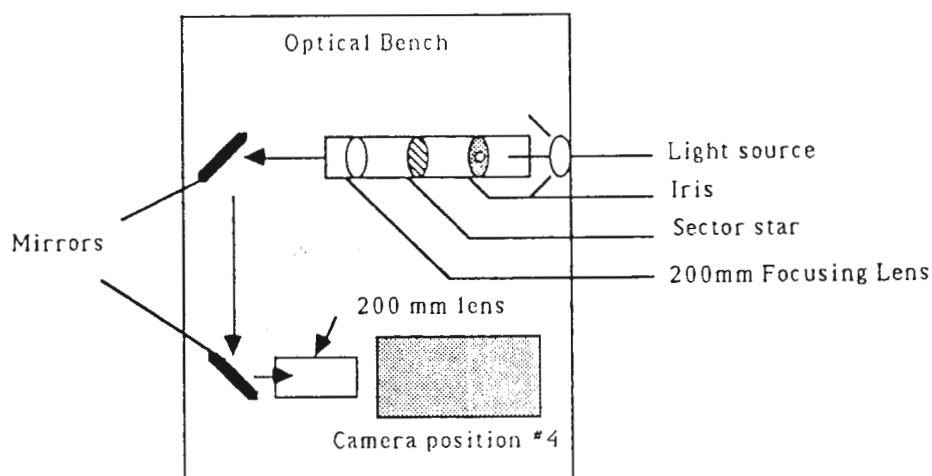


Figure 6: Object at infinity arrangement as setup on the optical bench.

The object at infinity setup uses simple geometric optics to create parallel light. A focusing device known as a sector star is placed at the focal point of a thin 200 mm lens. The sector star is then illuminated from behind by a point light source as created with an iris in front of a flashlight. The light rays that pass over the sector star and through the lens come out parallel; the condition for light coming from infinity. Two mirrors are then placed in the path of the light to reflect it onto the 200 mm lens in front of the camera. By adjusting the lens position one can bring the sector star into focus on the camera. At this point, the camera is at the focal point of the lens. The two focusing planes are now established, and they can be returned to by using the translational stage and the remote digital counter from the stepping motor. The above procedure can be performed at camera position #3 as easily as it was at camera position #4, and in fact was done during the experiment.

III. PRELIMINARY CONSIDERATIONS

A. COMPUTER SOFTWARE

As was mentioned above, the Macintosh II computer and the *Image* software are so vital to successful data acquisition and analysis that some remarks concerning their capabilities is warranted. Dallman [Ref. 9] discusses many of the options available in the software package, and demonstrates their use. The repeat of only those felt essential to this experiment will be done here. Although more current versions of *Image* are available, the one used for this experiment was version 1.14. It will be shown that this version has some limitations.

The Frame Grabber board and the *Image* software allow one to capture images from video cameras and video cassette recorders. The digitized images are then displayed on the computer screen in a black and white format with individual pixel intensities ranging from 0 (white) to 255 (black). Individual menus within the software allow the user to perform a variety of operations on the data obtained. These menus include data display options for viewing images in color or grayscale based on individual pixel intensities, functional options such as smoothing and noise reduction, editing options such as rotating and scaling images, and data analysis options such as line and three dimensional intensity profile plots. The software package is equipped with an information section that describes in great detail the use of each option available.

Two of the most useful editing options available in *Image* are the Invert command and the Selection Rectangle tool. The Invert command proves useful

when making three dimensional intensity plots. Dallman [Ref. 9] showed the difficulty in attempting to view a three dimensional plot of a non-inverted image of a laser beam spot. Since the laser beam spot is captured and displayed as a small white central region surrounded by larger dark region, a three dimensional intensity plot of a non-inverted image would "hide" the desired signal. If, however, the image is inverted prior to plotting, then the background appears white, and the signal is dark. Without prior mention of the use of the 3D Plot option, Figures 7 and 8 show the Invert command's usefulness. Since captured OTR images are displayed in the same format as described above for laser beam spots, one can see immediately the utility of the Invert command. The above statements apply equally as well when conducting line intensity / 2 dimensional profile plots. Recall that Figure 2 is a generic OTR line intensity profile.

Image allows the user to set the height and width of the captured images in a range from 32 to 2048 pixels. In this experiment, it was determined to use a height and width of 480 and 640 pixels, respectively. These dimensions were chosen due to the potential application of comparing experimental data with theoretical calculations using additional computer software. The Rectangular Selection tool allows the user to pick as an area of interest of any size within the 640 x 480 region. Once chosen, this area of interest may be manipulated and analyzed using all available software options. This technique proves especially useful in performing Integrated Density operations, a data analysis option to be discussed later.

The Density Profile and 3D Plot software options allow the user to see pictorially what the captured image looks like in two and three dimensions. When using the Density Profile tool a straight line may be drawn through any angle on the captured image and a line intensity profile similar to that

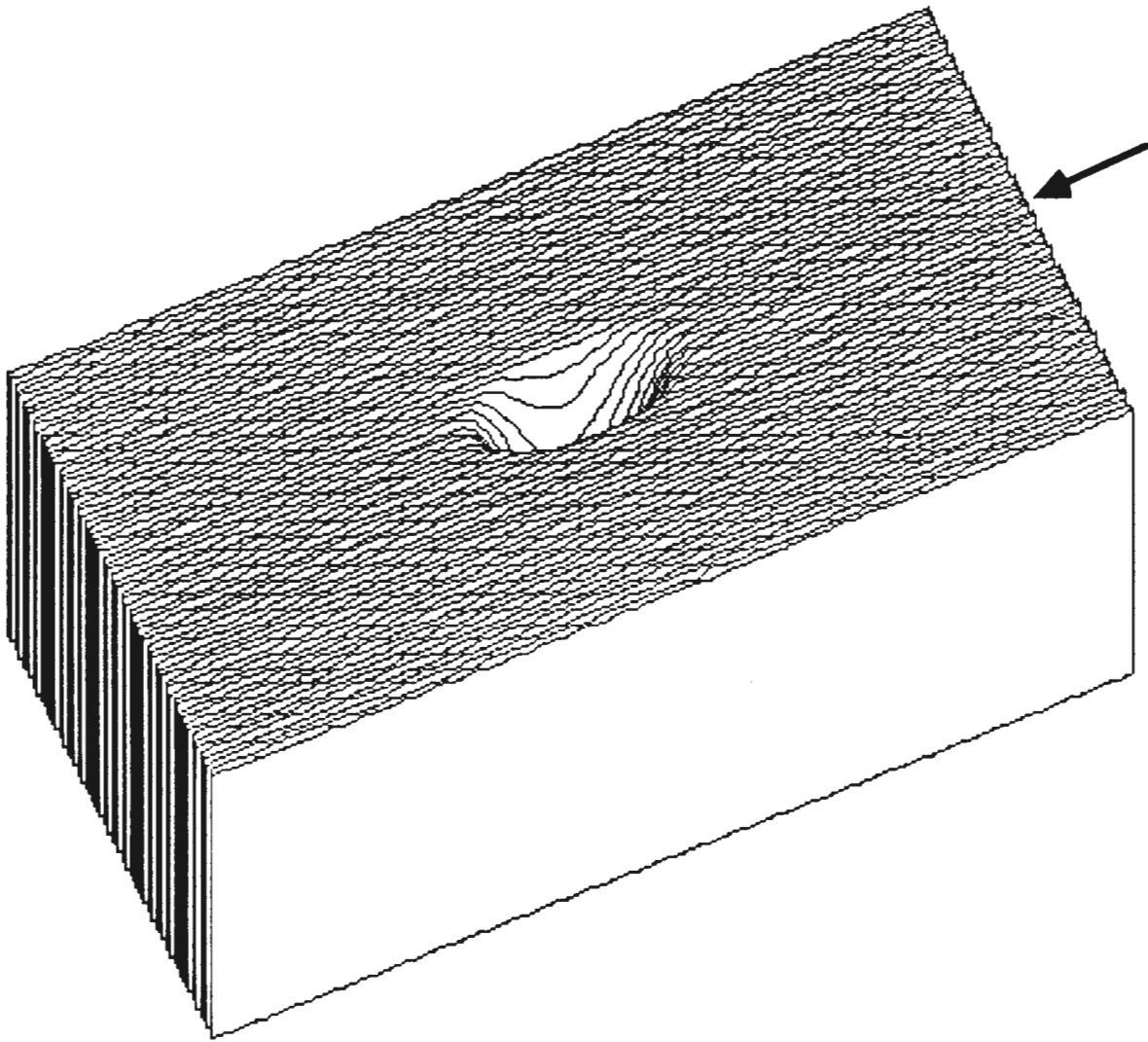


Figure 7: Three dimensional intensity profile plot of a Light Emitting Diode (LED). Image non-inverted prior to plot. The arrow indicates the location of the line scan shown in Figure 9.

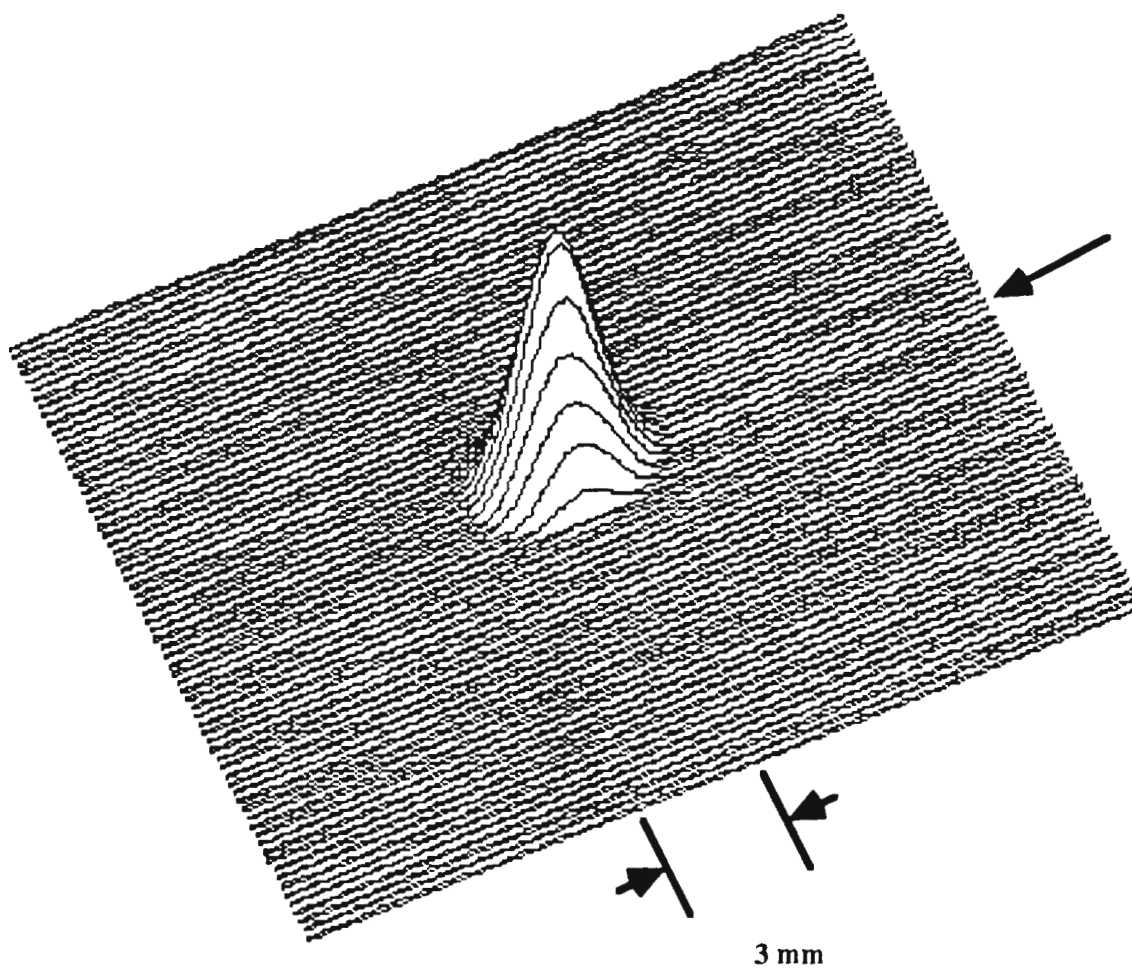


Figure 8: Three dimensional intensity profile plot of a LED. Image inverted prior to plot. (Note: same captured image as in Figure 7) The arrow indicates the position of the line scan shown in Figure 10.

in Figure 2 is generated. Unfortunately, the version of *Image* used does not allow the user to obtain individual data point information. As an example, Figures 9 and 10 show line intensity profiles of the same captured images shown in Figures 7 and 8. It can be seen that information concerning the

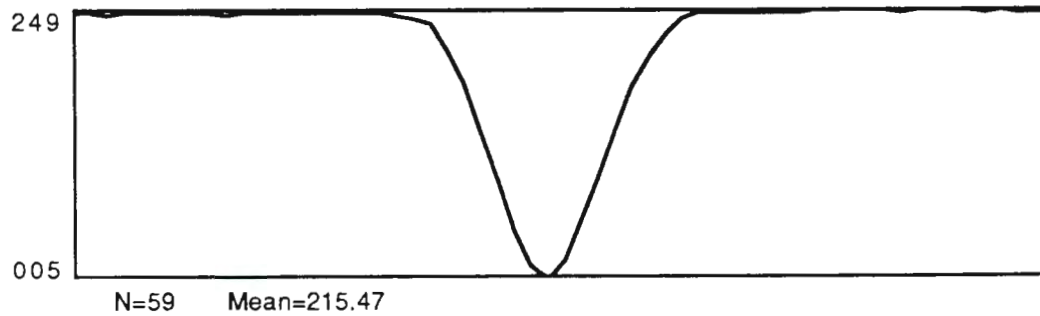


Figure 9: Density Profile plot of a LED. (Note: same captured image as Figure 7, where image is non-inverted prior to plotting.)

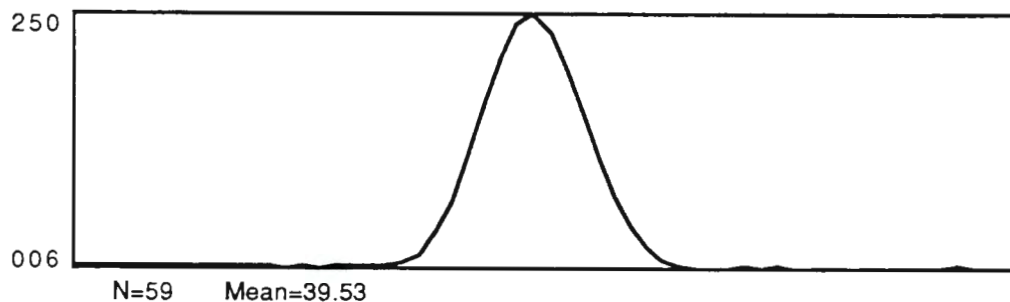


Figure 10: Density Profile plot of a LED (Note: same captured image as Figure 8, where image is inverted prior to plotting.)

range of pixel intensities is plotted on the vertical axis, while the length of the line scan is plotted on the horizontal axis. Also shown is the mean intensity for

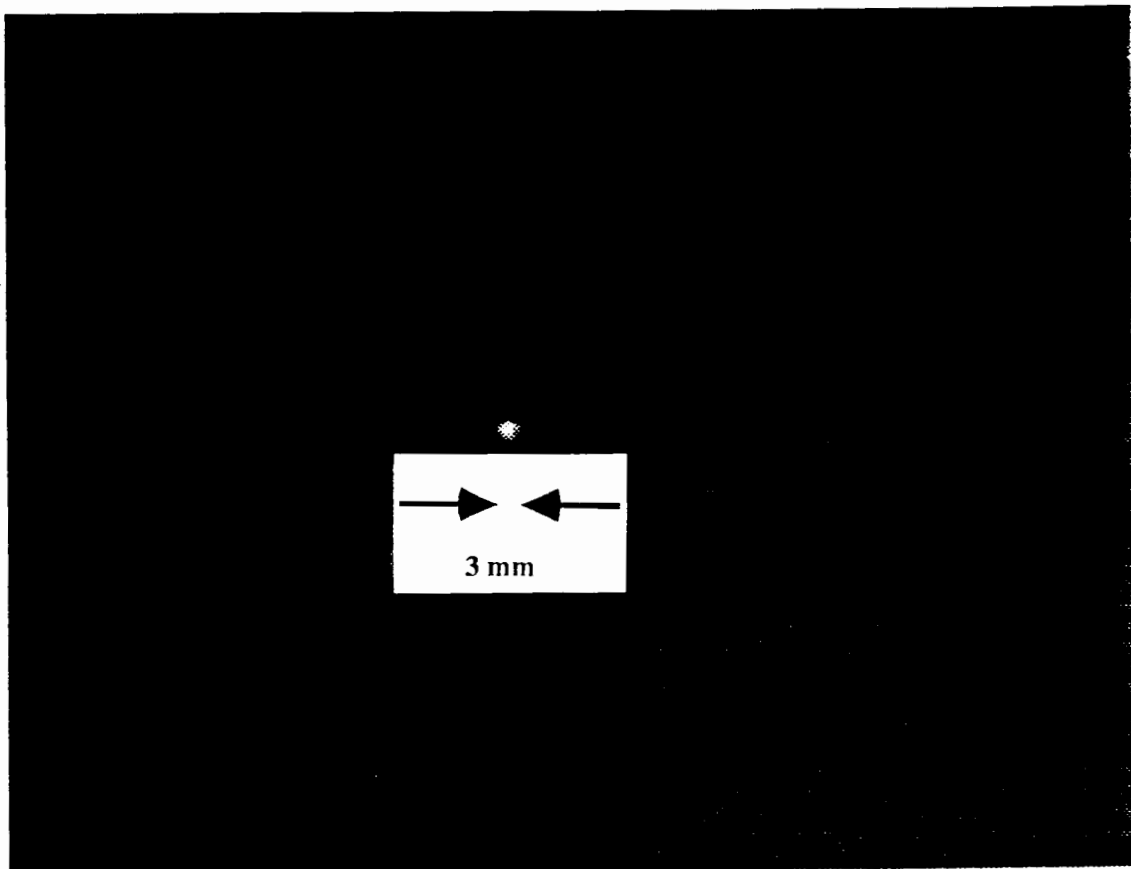


Figure 11: Captured image of LED as actually displayed on the computer screen. Inverting the image would produce a central dark region surrounded by a white region.

the scan. However, the individual pixel intensity values are not obtainable from the plot. In communication with the author of the software [Ref. 10] it was learned that *Image* version 1.14 does not allow the user to obtain this information, but that future versions did. The requirement for specific pixel data will be discussed in the next section of this report. *Image* does allow the user to identify specific pixels and associated intensity values by using the cursor. This "manual" method was used to calculate software / equipment accuracy based on the known intensity of a light source, despite the fact that it was extremely time consuming. The usefulness of the Density Profile tool will be shown in the analysis of the captured radiation cone OTR where, because of equipment limitations, the OTR image intensity differs only slightly from the background. The resulting two dimensional line intensity profile shows clearly the expected double hump.

The use of the 3D Plot option is essential in visually understanding captured images. Figure 8 showed the three dimensional intensity plot of a LED. Figure 11 shows the same captured image as it was displayed on the computer screen, only reduced in size for data presentation purposes. One can see that it is difficult to distinguish from the actual image the exact nature of the signal. Specifically, it would be hard for one to determine if there is a central region of peak intensity, and if so what is the magnitude of that peak. Also available with the 3D Plot option is the ability to rotate the captured image so that a 360° view may be obtained. Figures 12 and 13 depict the usefulness of the Rotate command in giving the user this full view, by showing three dimensional plots of two LED's placed side by side. Figure 12 shows the actual image as it appeared, while Figure 13 shows the same image rotated 90° to the right. As will be shown, the 3D Plot option proved especially useful in showing the intensity profile of electron beam spot OTR images.

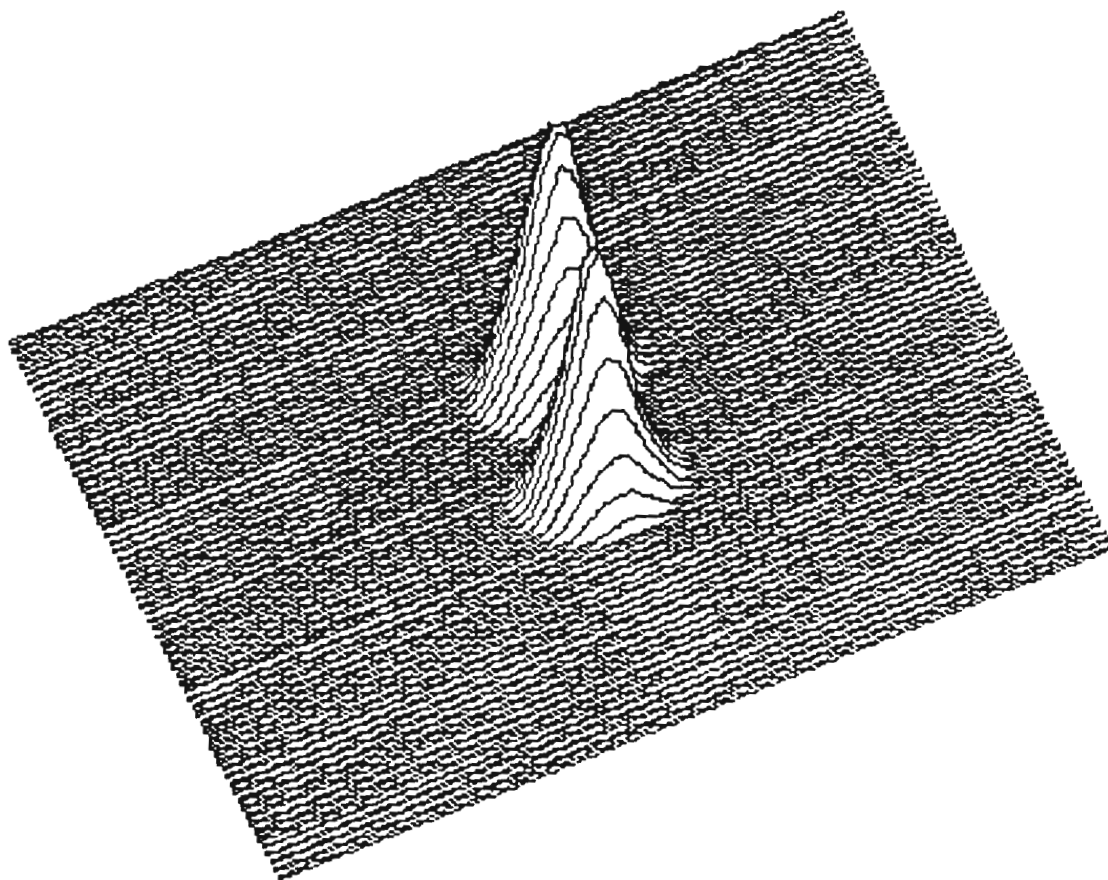


Figure 13: Three dimensional intensity plot of two LED's placed side by side. (Note: Same captured image as Figure 12 only rotated 90° clockwise prior to plotting.)

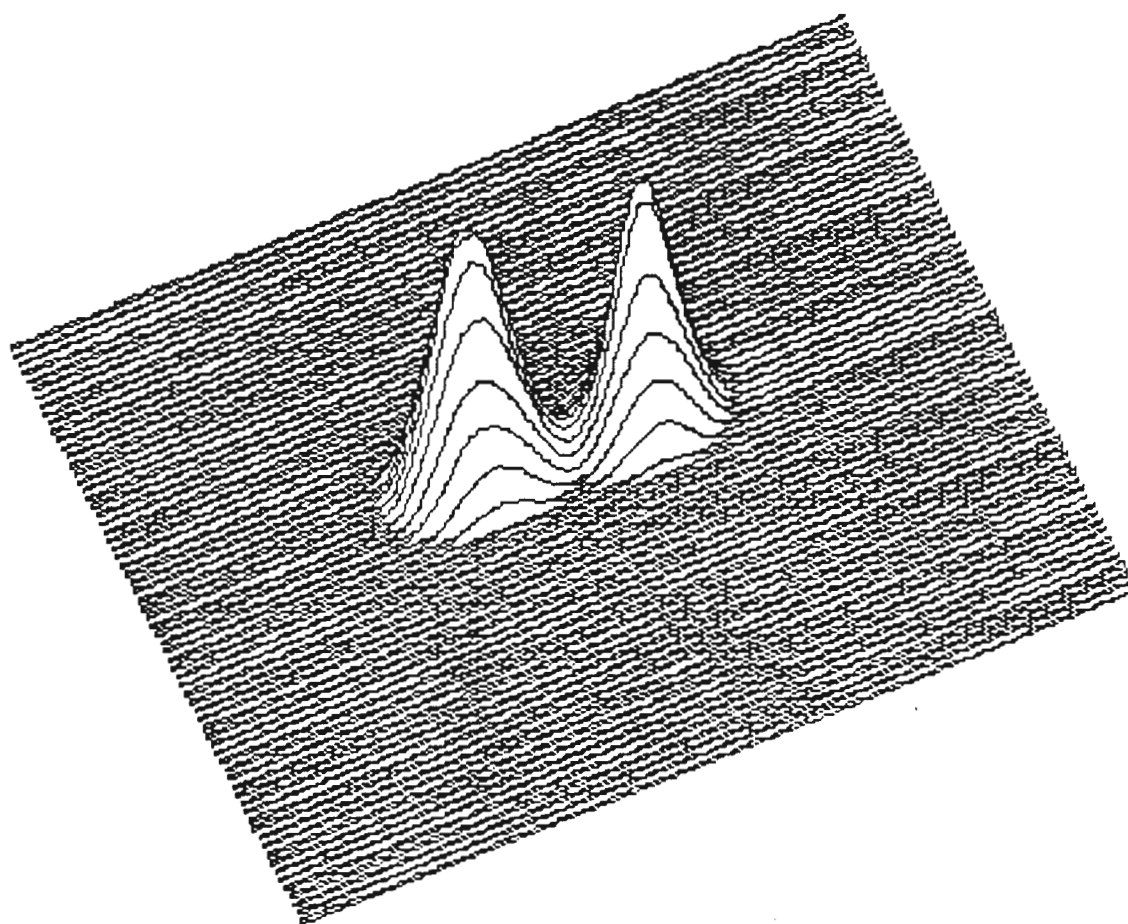


Figure 12: Three dimensional intensity plot of two LED's placed side by side.

The last two data analysis tools to be discussed are the Set Scale and the Integrated Density options. The Set Scale option allows one to calibrate the computer screen pixel units by using a dimensionally known length on a captured image. As seen in Figure 14, a cross hair enclosed by a circle of known diameter was drawn on the face of a phosphorus screen placed on the rotatable ladder. The ladder was then rotated so that it was perpendicular to a camera placed at position #3. By using the cursor and a Ruler tool, a line was drawn from one side of the circle to the other, and the dimensionally known length was typed into the computer. All future length measurements are then automatically computed in the same units. This function will prove useful in comparing the size of electron beam spot images produced both from phosphorus screen and OTR targets. By using a second dimensionally known length while focused at infinity, a calculation of the Lorentz factor is possible.

The Integrated Density function is *Image's* method of assigning a number to a given signal. Specifically, it integrates all pixel intensities within a given area of interest while at the same time accounting for the background. It is calculated using the following formula,

$$\text{Integrated Density} = (N * \text{Mean Density}) - (N * \text{Background Density}) \quad (\text{Eqn.2}),$$

where N is the number of pixels in the selection, and the Background Density is the most frequently occurring intensity value within the same selection. Dallman [Ref. 9] used the Integrated Density function extensively in attempting to distinguish the captured signal from the background. He encountered two obstacles though; TV camera response and light source constancy. In this experiment, having overcome both obstacles, the power of the Integrated Density function will be shown.

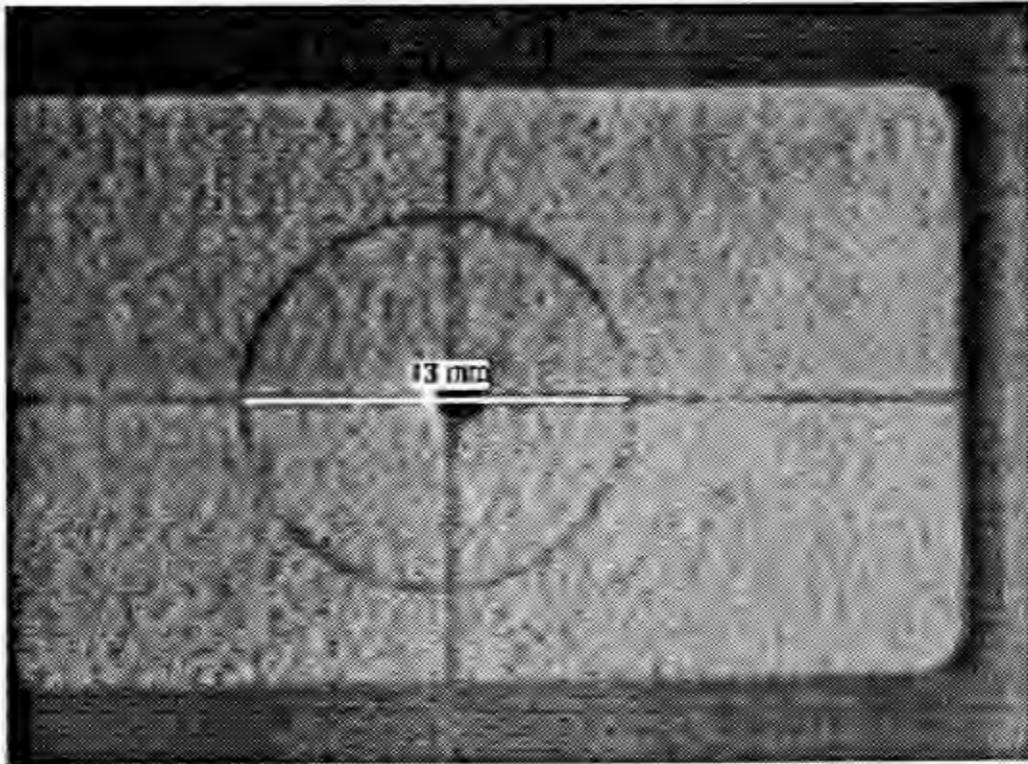


Figure 14: Cross hair and circle drawn on a phosphorus screen used for calibrating the computer screen pixel units.

B. EQUIPMENT CAPABILITIES

1. A Constant Light Source

In his attempt to determine camera response, Dallman [Ref. 9] found that by using the Integrated Density function on successive images of the same laser beam source, a variation in relative intensity of 10 - 15% was obtainable. By using an additional software option, namely the Average Frames function, he could reduce this variation to 3%. This fell short of the established goal of variations of less than 1% as required for precision experiments. As mentioned above, this shortcoming was attributed to two things, one of which was the source of light. It was found that the laser utilized was not mode-locked, and therefore it changed polarity frequently during operation causing instabilities in the captured images. In this experiment, a truly constant light source was sought after, and found in the form of a standard Light Emitting Diode (LED). A small, red light LED connected to a power supply was placed in a "black-box" arrangement (a wood box painted on the inside with non-reflective black paint). A photodetector connected to a fiber optics power meter was also placed in the box. Figure 15 shows the setup.

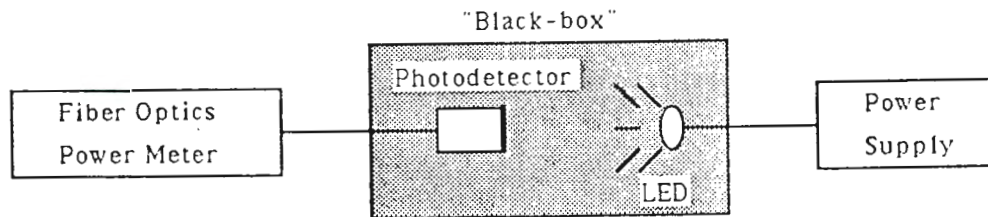


Figure 15: "Black-box" setup to determine absolute intensity of a LED.

The fiber optics power meter has the ability to measure absolute intensity of a given light source. With this setup, it was determined that the LED was

constant in intensity to within 0.1%. Having eliminated this first source of instability, it was time to determine camera response.

2. Camera Response

Recall from above that a "manual" method for determining equipment capabilities was mentioned. Instead of using the Integrated Density function it was determined to manually select specific pixel locations within a captured image for the purpose of recording intensity values. By selecting pixels whose individual intensities ranged from 0 to 255, one could establish the capabilities of the camera over the entire intensity spectrum. The procedure was carried out using the LED / black-box arrangement of Figure 15 with a camera replacing the photodetector. Two cameras were utilized; the COHU and the RCA Vidicon used by Dallman [Ref. 9]. In order to insure that the light from the LED spanned the entire intensity spectrum and at the same time did not completely saturate the camera, neutral density filters were placed immediately in front of the LED. An initial image was then captured, and the intensity and position of the most intense pixel was recorded. Next, pixel locations whose intensities were 90%, 50%, and 10% of the maximum were also recorded. Lastly, a pixel location that was far from the signal that could serve as the background was recorded. A series of images were then successively captured of the same LED, and the intensity at the above mentioned pixel locations was recorded. For the COHU, the error or noise level was determined to be ± 1.5 intensity units. For the series of LED images captured the peak intensity recorded was 250 and the background intensity was typically about 10. The noise level therefore corresponds to a 0.6% error at maximum intensity, 0.66% error at 90% maximum, 1% error at 50% maximum, 6% error at 10% maximum, and 15% error in the background. The same procedure carried out using the RCA Vidicon camera produced drastically different results. The noise level for this

camera was determined to be ± 7.5 intensity units. For this series of LED images, the peak intensity was 244, and the background was typically 15. Therefore the corresponding errors at maximum, 90%, 50%, and 10% of maximum and the background are 3%, 4%, 6%, 27%, and 54%, respectively. These results clearly show the inability of the RCA Vidicon camera to meet established goals for precision. The COHU on the other hand, shows that for a constant light source, intensity values on the order of 130 and higher, that is greater than 50% of maximum intensity, have a variation of less than 1%, and that even background intensities have a variation of only 15%. Intrinsic to these results is the fact that even for images captured in the black box, the background or most frequently occurring intensity was non-zero for both cameras. From this data, it was determined that only the COHU camera would be utilized for obtaining quantitative OTR images.

As a final check on the ability of the COHU and the software, neutral density filters of higher ND number were placed in front of a LED for successive captured images. An increase in ND number of 0.1 equates to a corresponding decrease in transmitted intensity of 26%, a result that was not seen by Dallman when using the RCA Vidicon [Ref. 9]. Results that agreed quantitatively (26% - 29%) with expected reductions were seen however, when using the COHU. These reductions were seen both when using the procedure of selecting individual pixels as well as when using the Integrated Density function.

IV. EXPERIMENTAL RESULTS

A. RESULTS

The initial goal of the experiment was to capture OTR images with the COHU placed at camera position #4 and focused on the foil. On two separate occasions with beam energies of 25 MeV and 60 MeV, as limited by accelerator capabilities at that time, OTR was not seen. On the next attempt, however, with a beam energy of 100 MeV a glimpse of some white light appeared on the computer screen. Referring to Figure 2, the peak intensity is a function of γ^2 , so it is suspected that imaging capabilities were insensitive to the lower energy OTR. Using the electron beam focusing magnets, this light was focused until a sharp, beam spot OTR image appeared. Figure 16 shows the captured image as well as a three dimensional plot of the OTR pattern. As can be seen, the image is completely saturated in the center. In order to eliminate this saturation, the beam current was decreased until a non-saturated image appeared. It should be mentioned here that the Secondary Emissions Monitor (SEM) used for measuring beam current was not calibrated, so the actual beam current was not known. The SEM efficiency is approximately 2%. A later section of this report will show that despite this, a calculation of beam current based on captured OTR images is still possible. Figure 17 shows the effect of decreasing beam current. Note that although the image is not saturated, there appears to be two areas of maximum intensity within the beam spot. The three dimensional plots shown in Figures 18 and 19 verify this double peak. Although this result was not expected, it reappears frequently, and therefore gives one a feel for the quality of the electron beam.

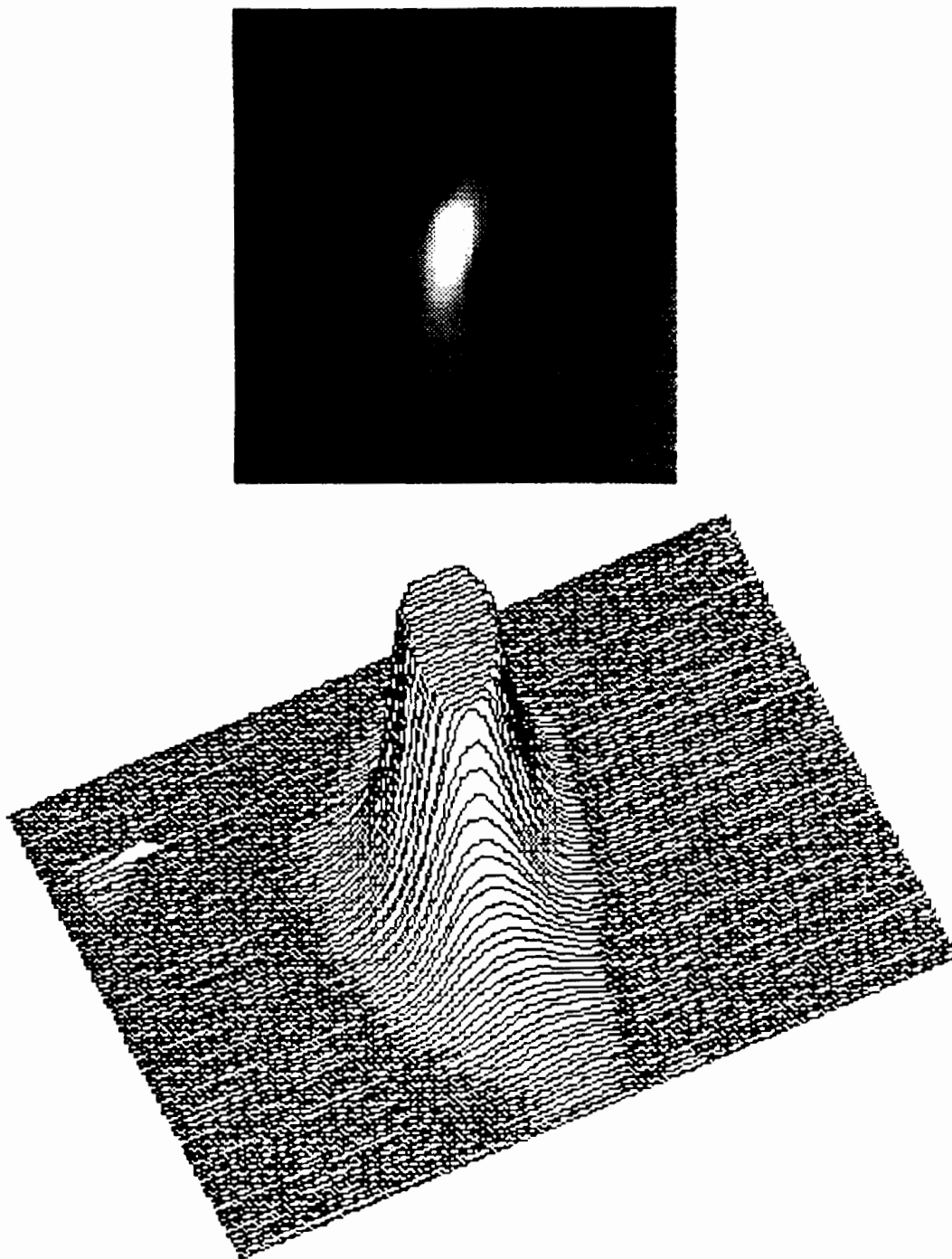


Figure 16: Electron beam spot OTR from foil in the secondary chamber and accompanying three dimensional plot. Note the saturation and elliptical shape. (COHU camera at beam energy of 100 MeV and uncalibrated current of approximately 0.5 μA .)

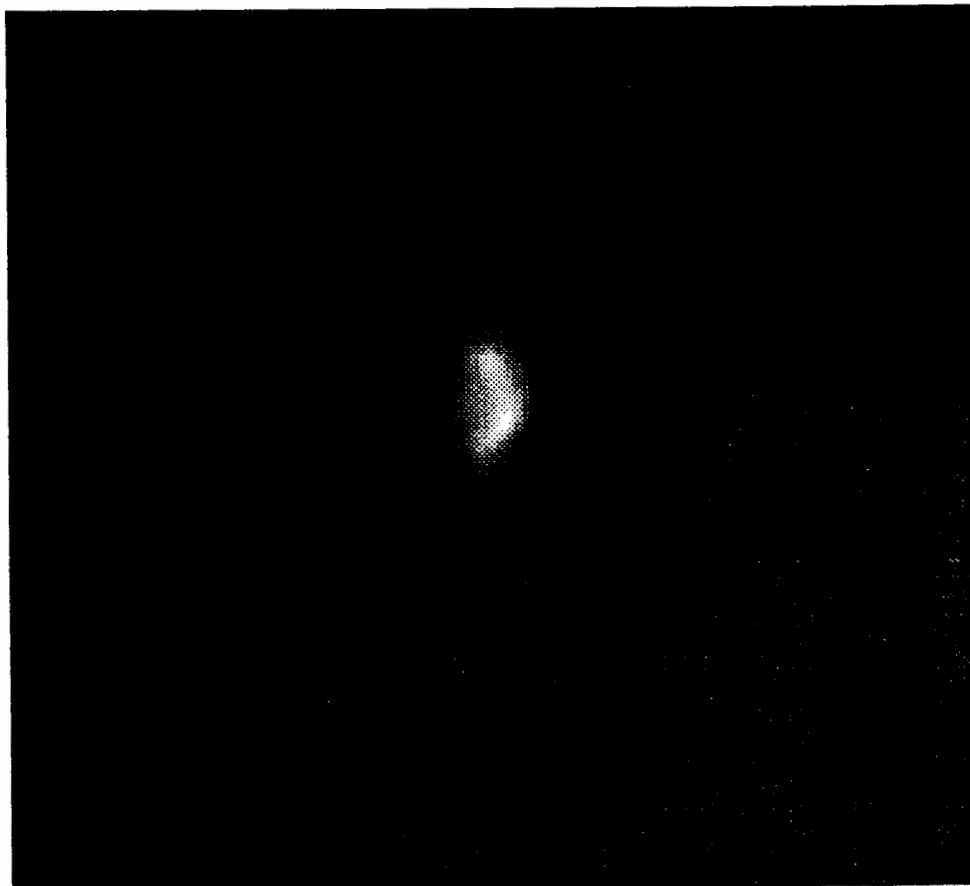


Figure 17: Electron beam spot OTR from foil in the secondary chamber. Note the appearance of two peak intensity points. (COHU camera at beam energy of 100 MeV and beam current less than 0.5 μA .)

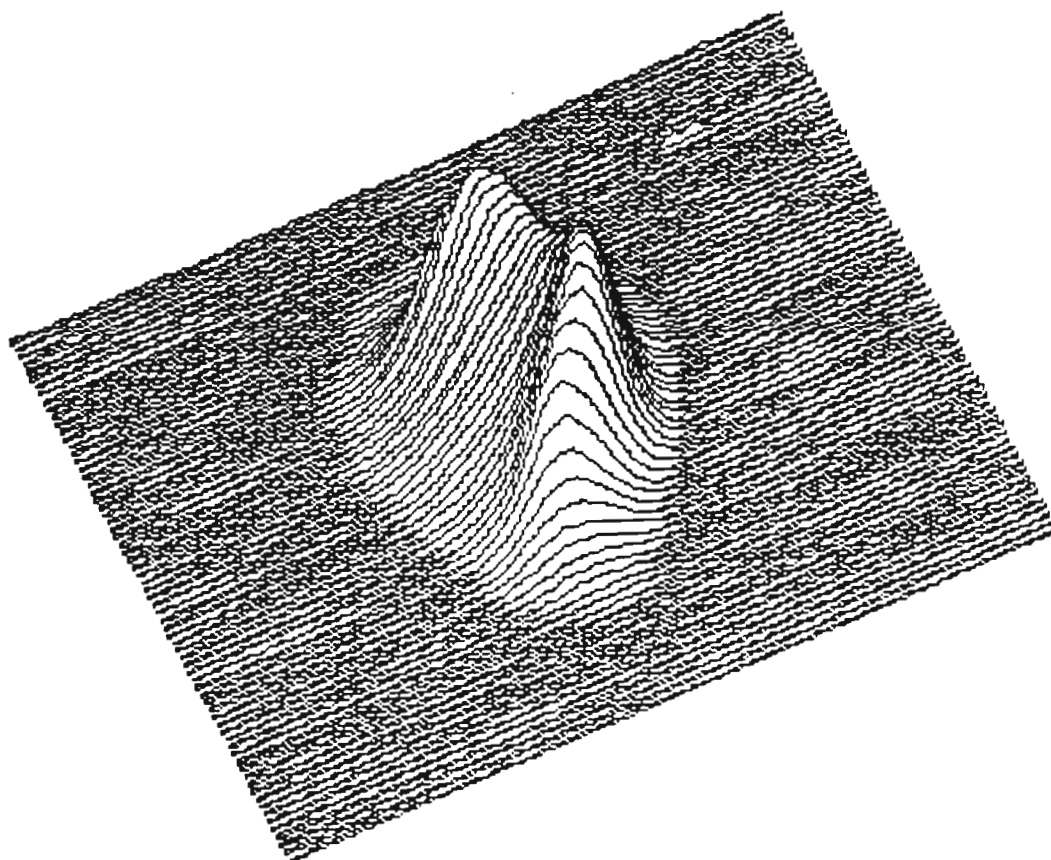


Figure 18: Three dimensional plot of electron beam spot OTR shown in Figure 17. Note the two peak intensity points.

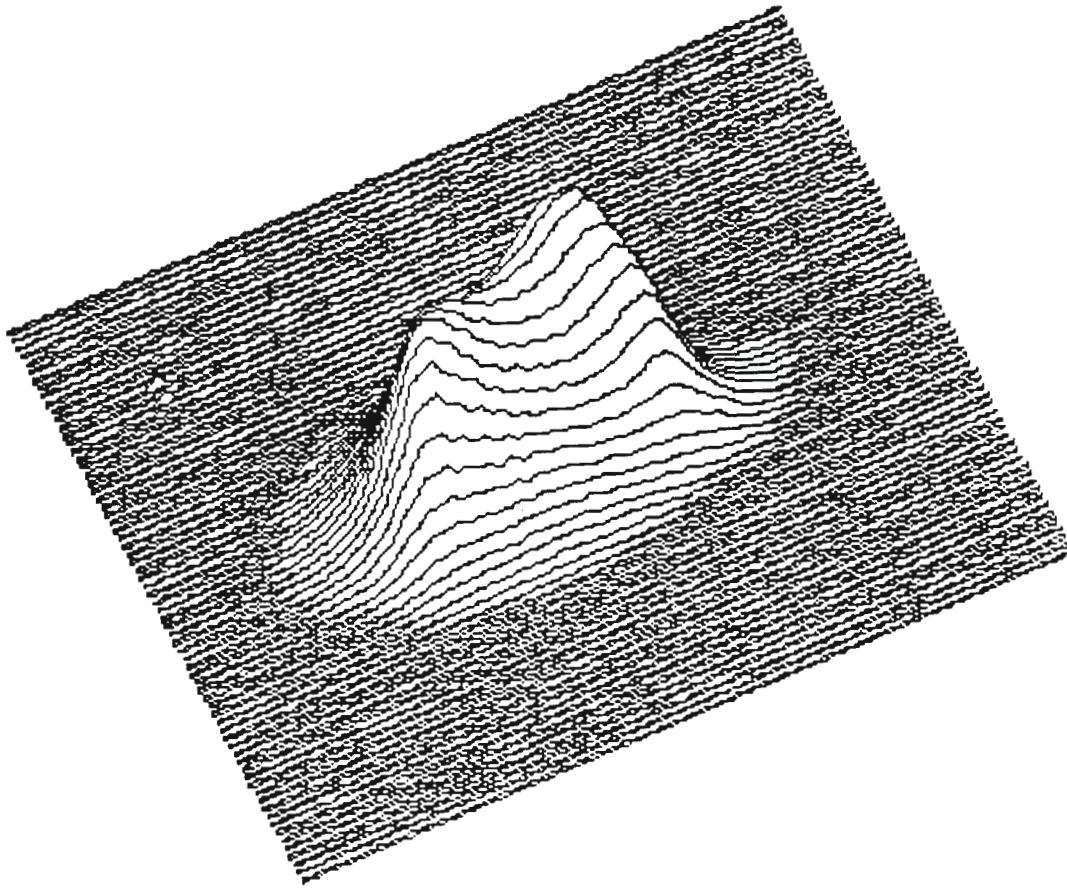


Figure 19: Three dimensional plot of electron beam spot OTR shown in Figure 17, rotated 90° clockwise prior to plotting. Note two peak intensity points.

Another peculiarity can be seen in Figure 16. Specifically, the beam spot is not circular in shape, but rather is elliptical with the longer axis in the vertical direction. Since the vertical plane of the foil in the secondary chamber is perpendicular to the beam axis while the horizontal plane is oriented 45° to the axis, this vertical elongation of the beam spot is inexplicable from geometric optic considerations. In an attempt to eliminate this effect, the electron beam steering and focusing magnets were used extensively but to no avail. The beam spot shown in Figure 16 is the sharpest one that was obtained. This proved to be an area of some concern, and in fact dictated the need for OTR analysis of targets in the primary chamber. During the accelerator start-up and beam alignment procedure, it was noticed that the beam spot generated on the phosphorus screen in the primary chamber was tighter and more circular than on the foil OTR pattern. Although this was seen with a less sensitive camera and lower magnification lens, it was determined that the COHU and 200 mm lens should be placed at camera position #3 for future OTR measurements in this experiment.

Prior to changing the initial configuration though, more OTR images were captured from the foil in the secondary chamber. Two goals were established. First, it was decided that a series of beam spot OTR images would be obtained for a variety of beam currents. Using the *Image* software, some formal dependence of OTR on beam current might be obtained. Second, a series of OTR images would be captured under the same beam parameters in order to identify the constancy of the electron beam.

For the first goal, a beam energy of 100 MeV was established and 35 subsequent beam spot OTR images were captured for currents ranging from 10nA to 2 μ A. Using *Image*, graphs of Integrated Density versus beam current were generated. Figure 20 shows a plot of the integrated density of the entire

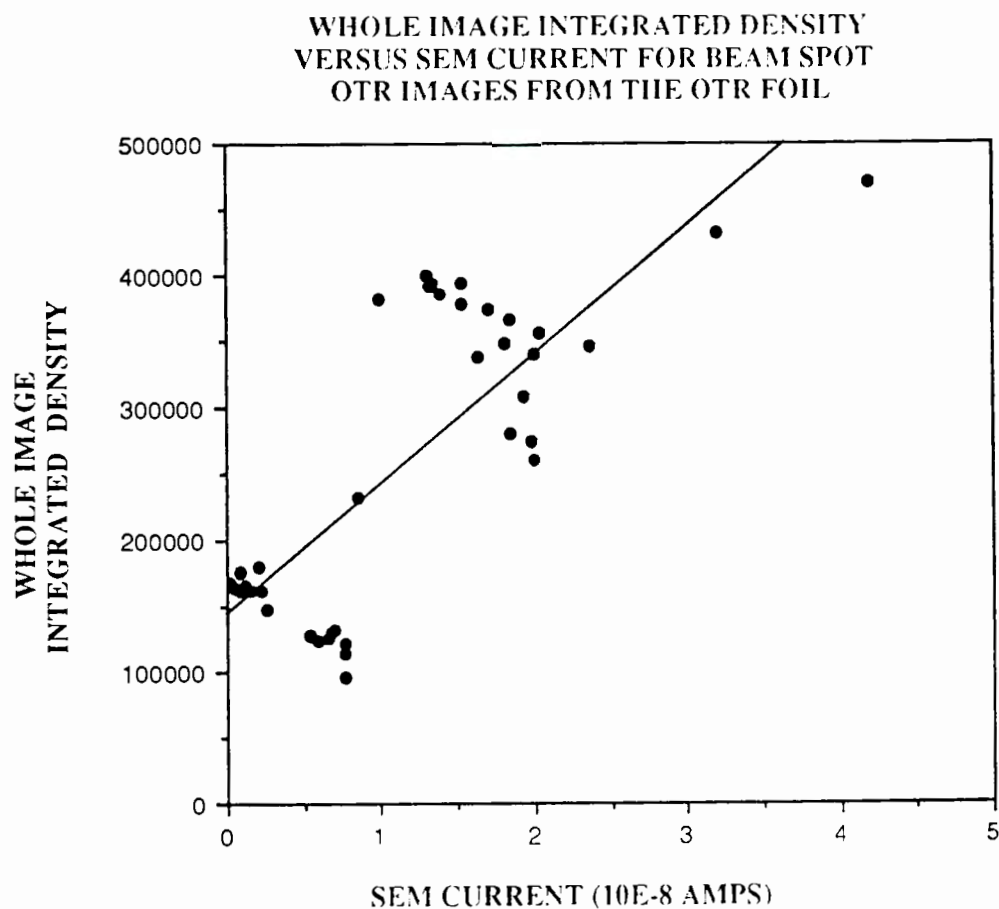


Figure 20: Plot of entire image integrated density versus SEM current for beam spot OTR images from the OTR foil. Beam energy 100 MeV.

captured image as a function of the SEM current. The horizontal scale is the observed SEM current so the approximate beam current is obtained by multiplying by 50. It can be seen that a poor linear relationship exists. Intuitively, one might guess that since this plot shows a poor linear relationship, so might a plot of the signal-alone integrated density versus beam current since the two differ only by a constant background. Figure 21 shows that this is not the case however, in that a plot of the signal or "area of interest" integrated density versus beam current is a straight line. *Image's* technique of quantifying a specific signal is therefore effective provided one uses the Selection Rectangle tool to select an area of interest around the desired signal. In order to see the dependence of the background on beam current, two techniques were adopted. First, the integrated density of a selected area around the signal was computed and the integrated density of a similar sized region in the background of the image was subtracted. The results are shown in Figure 22. As can be seen, a good linear dependence exists. However, several of the computed integrated densities are less than zero, a result that was not expected. In order to explain this, one must refer back to the definition of integrated density. Specifically,

$$\text{Integrated density} = (N * \text{Mean Density}) - (N * \text{Background Density}) \quad (\text{Eqn 2}),$$

where N is the number of pixels in the selection and the Background Density is the most frequently occurring intensity value within that same selection. The first factor on the right hand side of Equation 2 equates to the integrated density of the entire area selected. In comparing this factor alone for areas of interest containing signals to those containing only background, one can see that provided there is any sort of signal present, i.e., there exists at least a few

SIGNAL INTEGRATED DENSITY VERSUS
SEM CURRENT FOR BEAM SPOT OTR IMAGES
FROM OTR FOIL

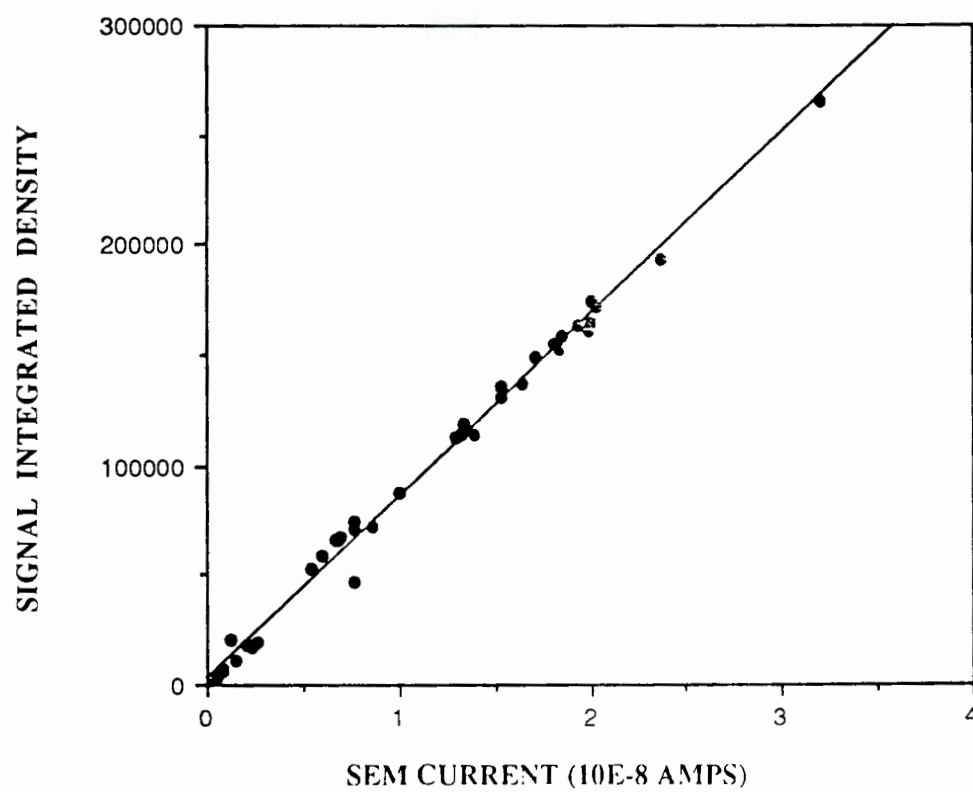


Figure 21: Plot of signal integrated density versus SEM current for beam spot OTR images from OTR foil. Beam energy 100 MeV.

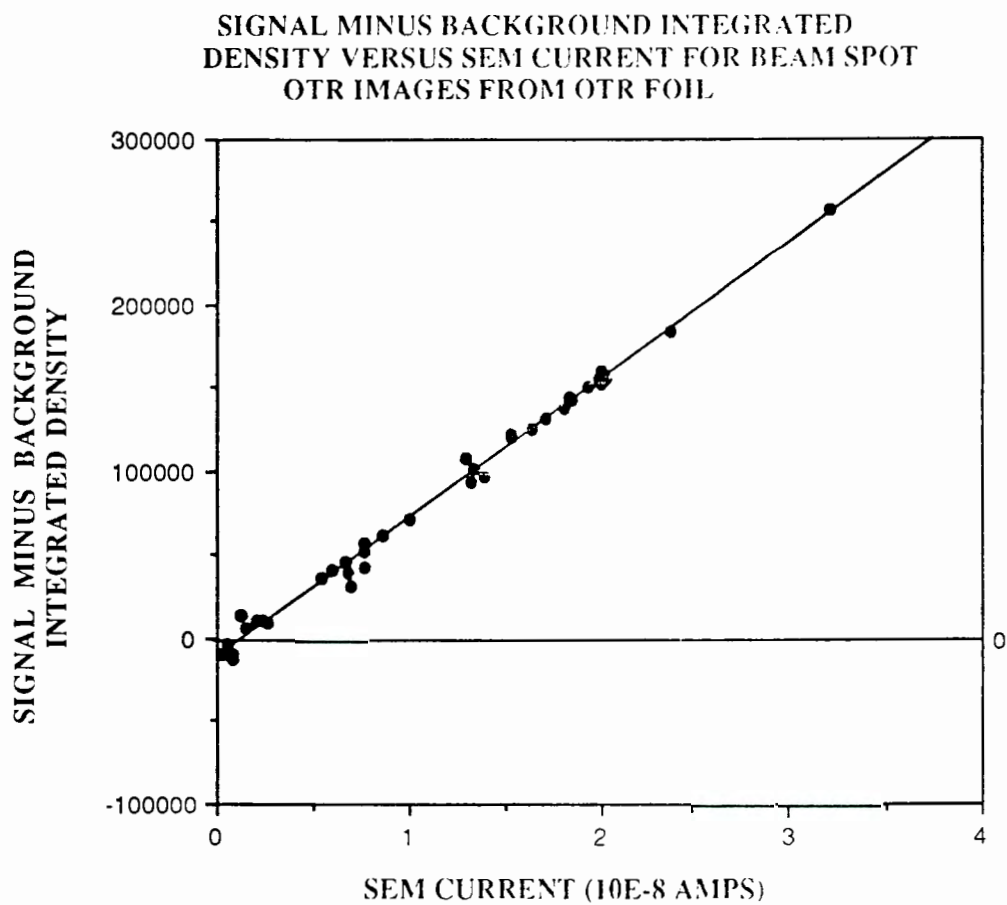


Figure 22: Plot of signal minus background integrated density versus SEM current for beam spot OTR images from OTR foil. Beam energy 100 MeV.

pixels within the selection whose intensity values are greater than the surrounding pixels, the signal integrated density will be greater than the background integrated density. The second factor on the right hand side of Equation 2 must therefore be the cause of the negative integrated density values in Figure 22. Recall from earlier discussion, that the background for images captured by the COHU is on the order of 10 pixel intensity units with variations of nearly 2 units. As an example, if one compares the second term on the right hand side of Equation 2, one can see that if the most frequently occurring intensity within a background region is 10 and that for a signal region is 8, then the difference of the two can produce negative integrated density values. This is in fact the reason for these negative values shown in Figure 22.

The second technique for evaluating the dependence of the background on beam current involves using the integrated density values of the background-alone areas. Figure 23 shows a plot of these integrated density values, normalized to the average, as a function of SEM current. The figure clearly shows that the background is not constant, and that variations as high as three times the average are possible. Another source of this non-constant background can be seen in Figure 24. In this three dimensional plot of a beam spot OTR pattern, a line appears through the top of the image. This line has an intensity greater than that of the background, and therefore causes some false background integrated density readings. The lines appeared at no specific times, and are thought to be caused either by some form of non-synchronization in experimental equipment, or perhaps from radiation effects on the electronics.

As a final check on the dependence of OTR image intensity on beam current, a technique similar to that for testing camera response was used. After the

COMPARISON OF BACKGROUND INTEGRATED
DENSITY FOR BEAM SPOT OTR IMAGES
FROM OTR FOIL

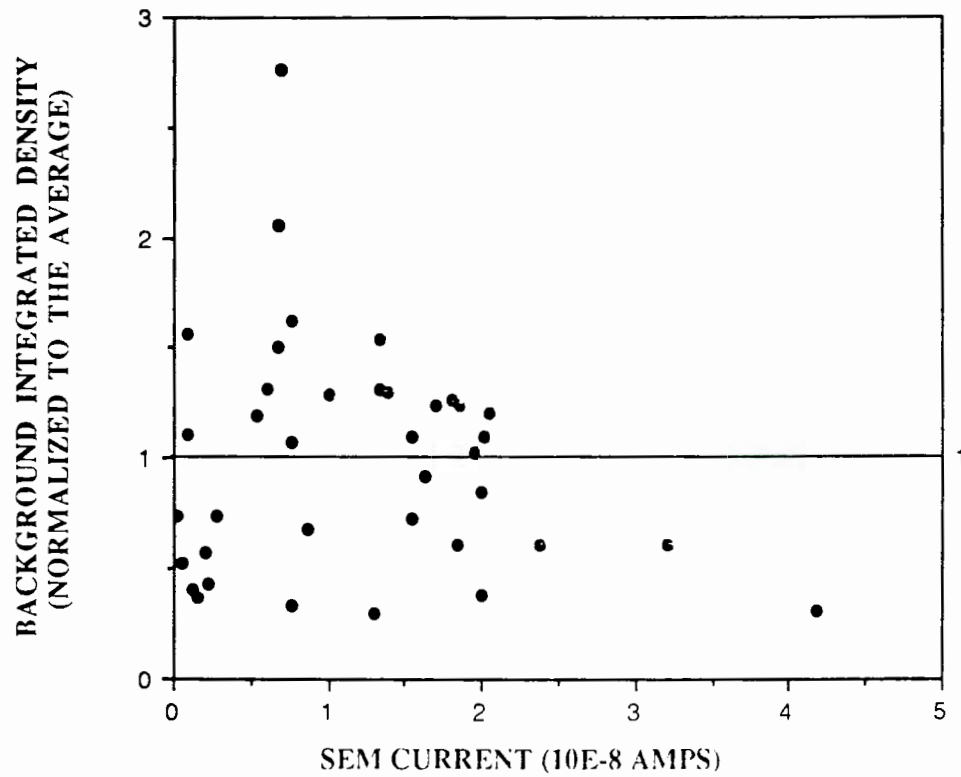


Figure 23: Comparison of background integrated densities for beam spot OTR images from OTR foil.

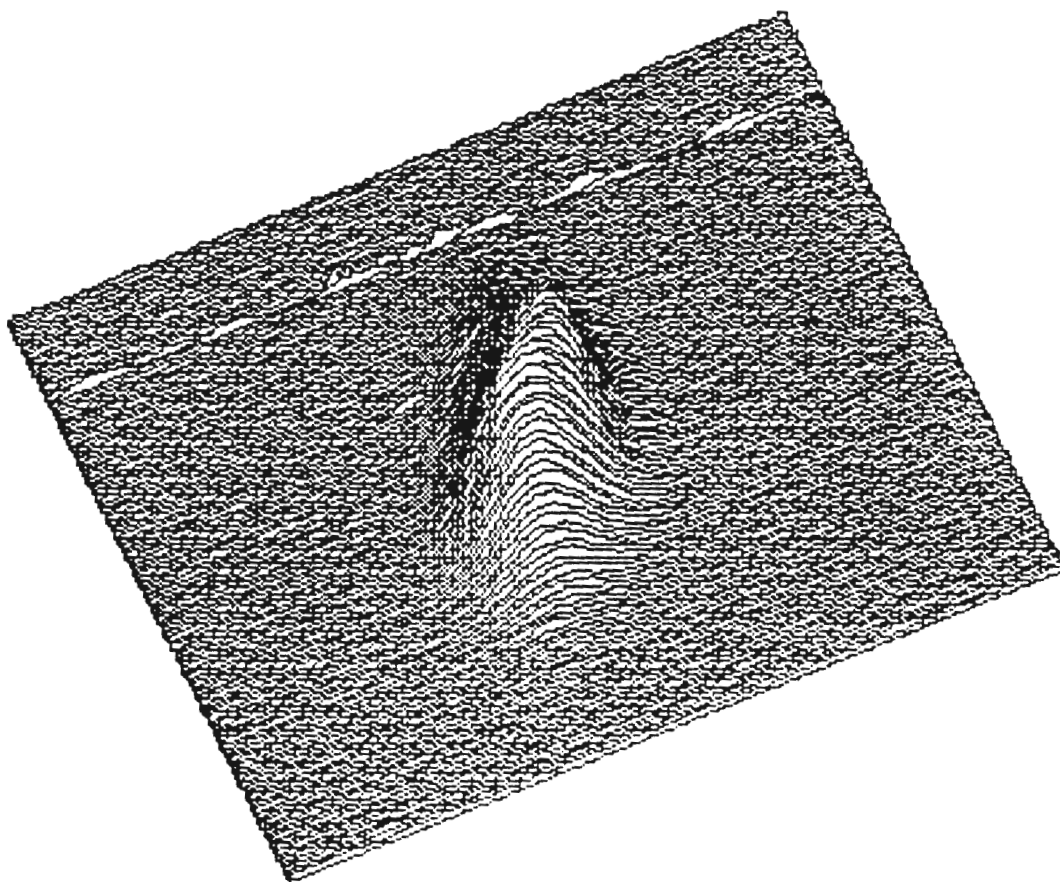


Figure 24: Three dimensional plot of a beam spot OTR image from the OTR foil with an interference line.

initial, high current beam spot OTR image was captured, pixel locations with nominal intensities of 100%, 90%, 50% and 10% of the maximum were recorded. The individual intensity values for these pixel locations were then recorded for various beam currents. The background intensity was subtracted from each of these values, and the data was plotted as a function of the observed beam current. The results are shown in Figure 25. As can be seen, linear relationships exist for the four different pixel locations. The points lie on straight line curves representing intensity ratios of 100 : 92 : 37 : 4 %. This result is expected since all pixel locations used are within the signal, and the signal integrated density plot in Figure 21 was also linear. The scatter of the data points in Figure 25 is a result of camera/computer limitations and, as will be shown next, variations in the electron beam itself.

The second goal for the initial camera setup was to determine how the electron beam changed under constant beam parameters. To achieve this, a beam energy of 100 MeV was established, and the beam current was adjusted such that the resulting beam spot OTR pattern was not saturated. Once accelerator conditions were relatively steady, four successive OTR images were captured. The time between each captured image was less than 15 seconds. The results are shown in Figure 26. In this figure are enlarged beam spot images as captured by the computer, as well as vertical two dimensional line scans through the regions of peak intensity. As can be seen from the actual images, the shapes of the OTR patterns are similar, but the internal structures are quite different. The line scans verify this result by showing that not only are the profiles different in shape, but also that the peak intensity is not constant. This indicates that the electron beam changes constantly. This discovery along with the fact that the beam spot images are not circular, indicates that the

PIXEL INTENSITY VERSUS SEM CURRENT FOR BEAM SPOT OTR IMAGES FROM OTR FOIL

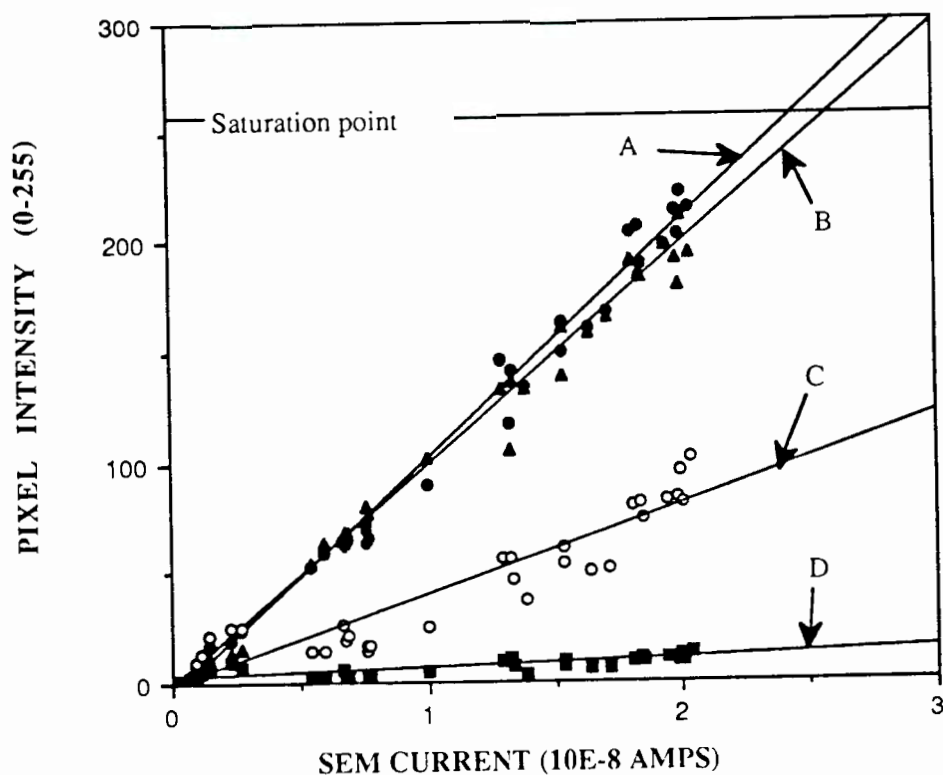


Figure 25: Pixel intensity as a function of SEM current for beam spot OTR images for OTR foil. Pixel locations are fixed and are referenced as a percentage of the maximum intensity of the beam spot generated at the highest beam current. A -100%, B - 92%, C - 37%, D - 4% of maximum intensity. Beam energy 100 MeV.

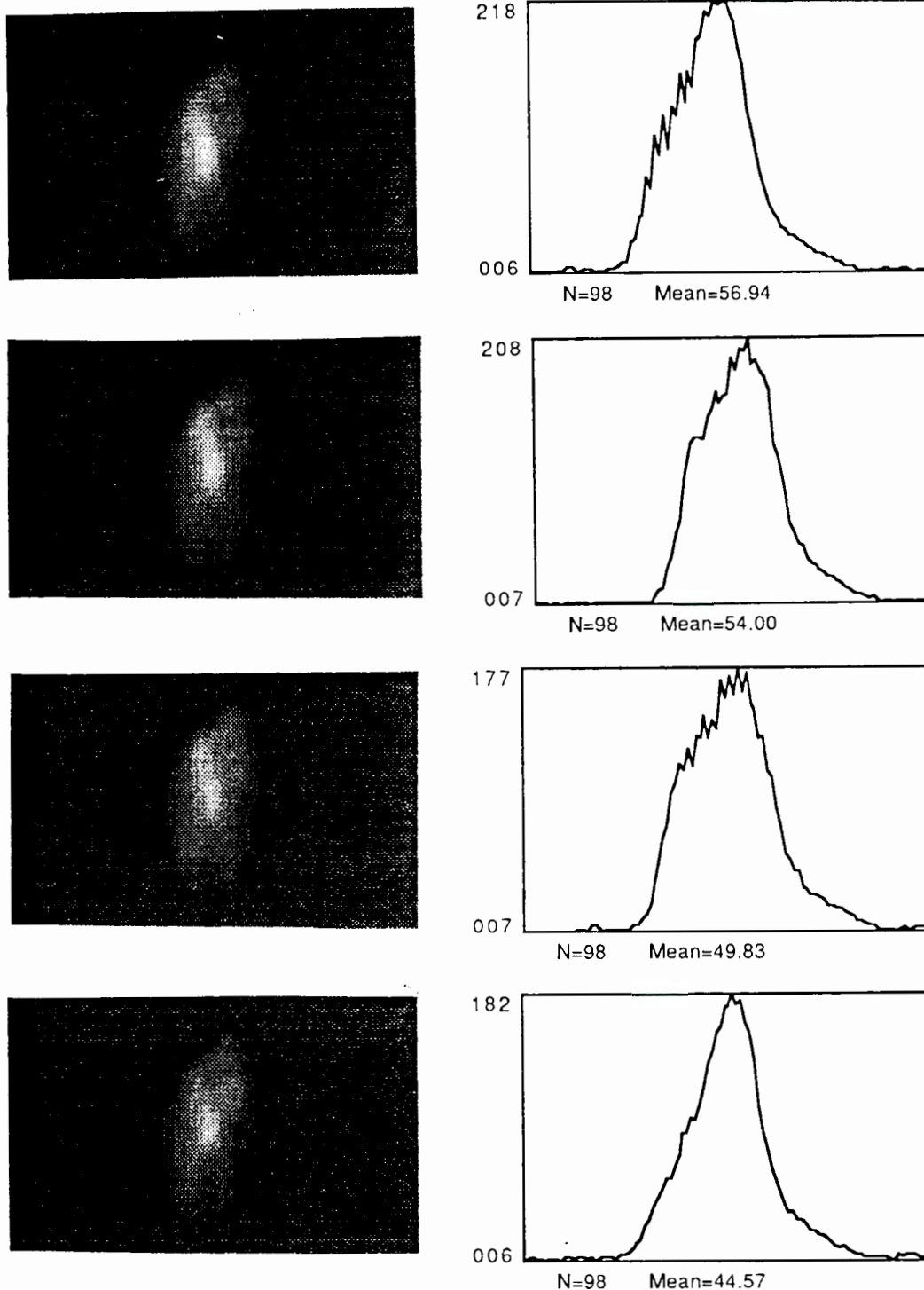


Figure 26: Comparison of beam spot OTR patterns and associated line intensity scans for constant accelerator parameters. Beam energy 100 MeV, images from OTR foil. The time between captured images is approximately 15 seconds.

quality of the electron beam is not ideal. However, both discoveries allow for future exploration.

It should be mentioned that an attempt at viewing the radiation cone OTR pattern at camera position #4 was made, but that no signal was seen. Initially, it was thought that this was due to inadequate alignment since the only common point of focus for the laser and the electron beam was the one in the primary chamber. As will be shown later, the lack of a radiation cone OTR pattern for this camera position was not due to misalignment.

Having captured all desired images at camera position #4, the COHU and 200 mm lens were placed at camera position #3. In addition, the camera normally used by accelerator technicians at position #1 was moved to position #2. This was done because the 100 mm lens associated with that camera would allow for close-up viewing of potential OTR images through that viewport. The alignment of this camera however, was done only visually since no extensive analysis of its captured images was foreseen. The accelerator was then started, with a beam energy of 96 MeV. Recall from above, that the purpose for moving the COHU to this position was to take advantage of the tighter beam spot generated on the phosphorus screen in the primary chamber. As can be seen in Figure 27, the resulting focused beam spot as captured by the COHU was not circular, although it was smaller than previously captured OTR images from the OTR foil. Equally important is the fact that the beam current for this image was about one-tenth that of the beam spot OTR pattern shown in Figure 16. This was because at higher currents, the beam spot on the phosphorus screen shows more extensive saturation. The target ladder was then adjusted so that additional targets could be placed in the line of the beam. Figures 28 and 29 show the beam spot OTR images of a gold foil and a front surfaced mirror, respectively. Again, the elliptical shape of the OTR pattern is visible in both

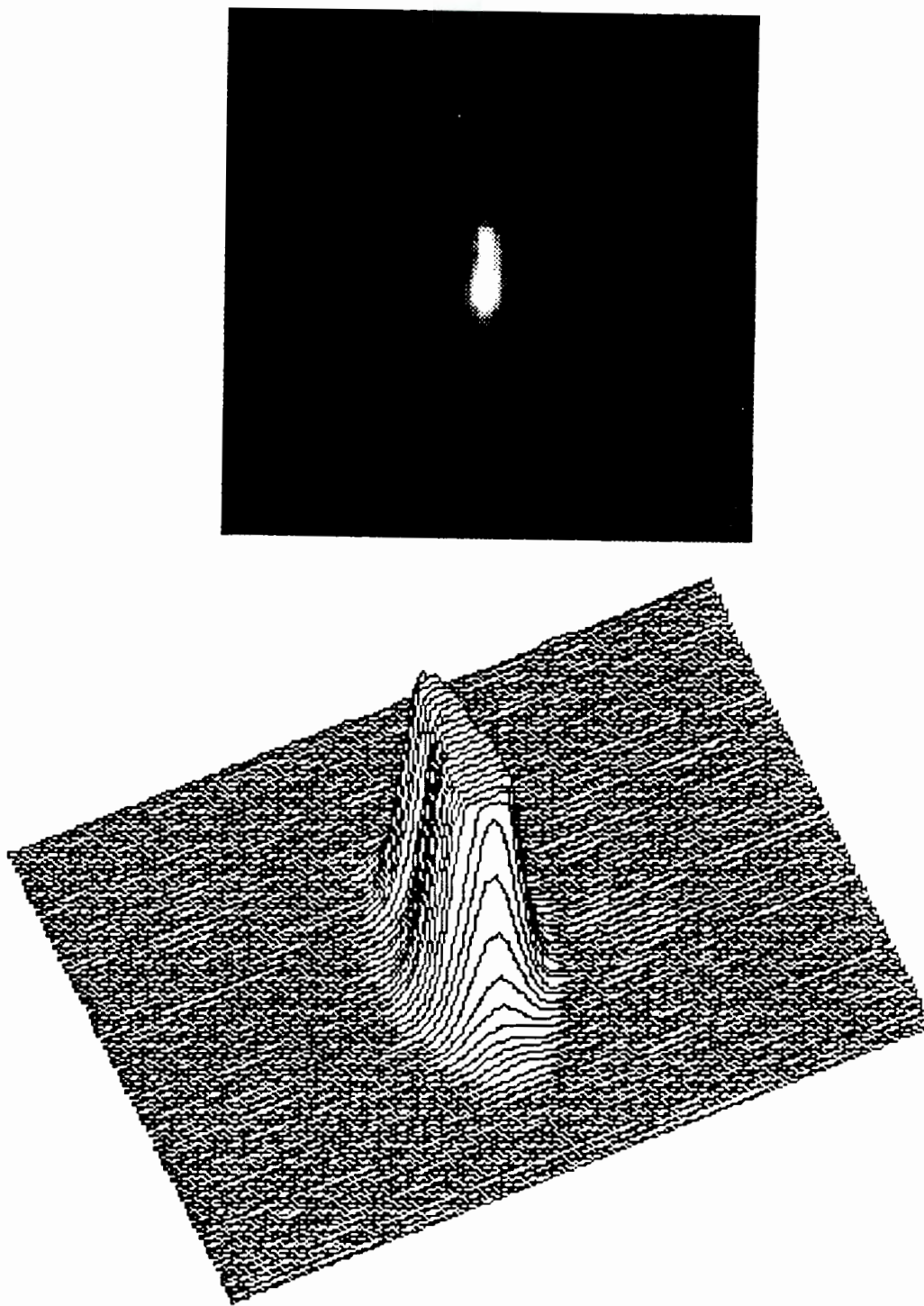


Figure 27: Phosphorus screen beam spot as captured by the COHU at camera position #3 and associated three dimensional plot. Note image saturation. Beam energy 96 MeV.

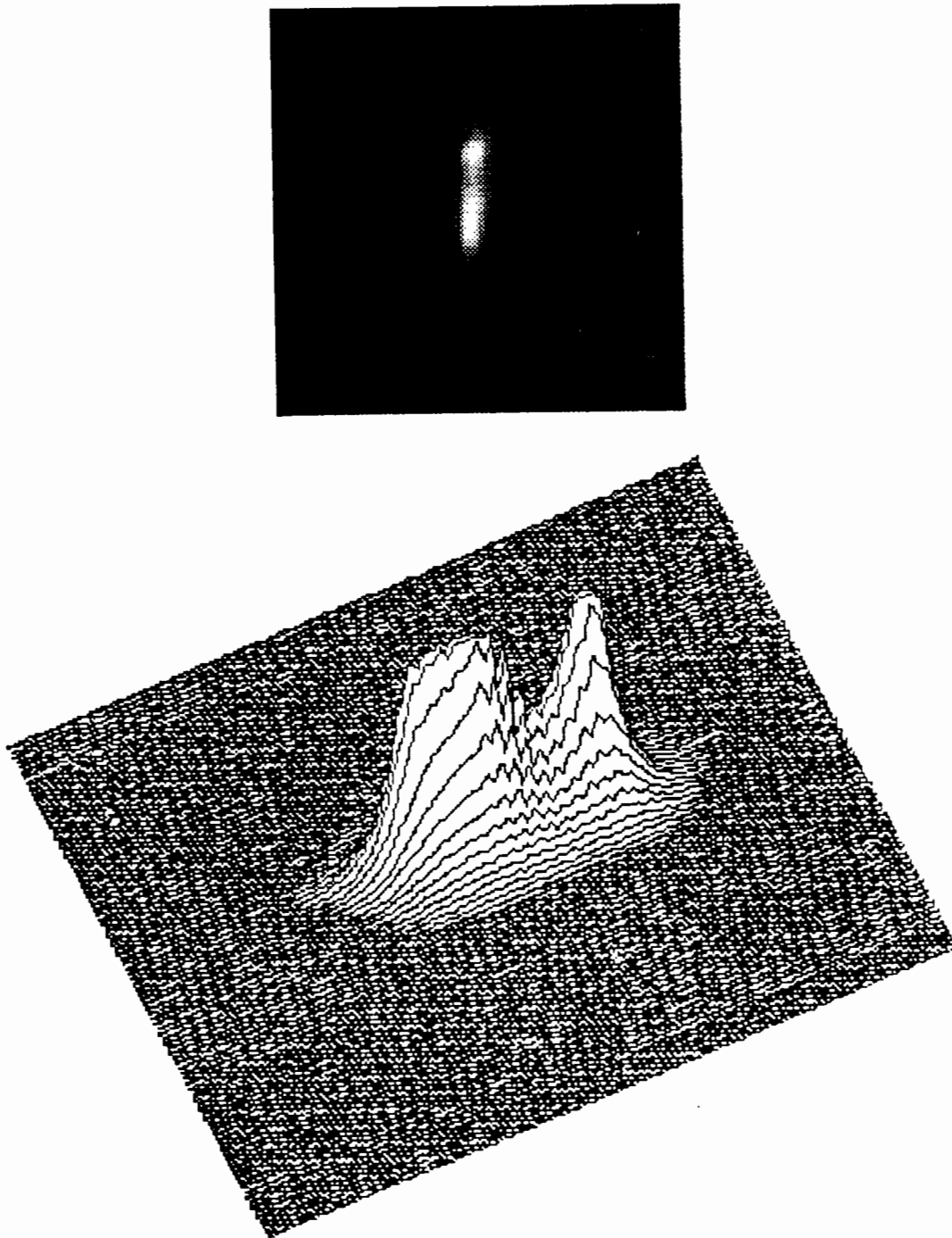


Figure 28: Beam spot OTR pattern from a gold foil in the primary chamber and associated three dimensional plot rotated 90° clockwise prior to plotting. Note double peaked intensity. Beam energy 96 MeV.

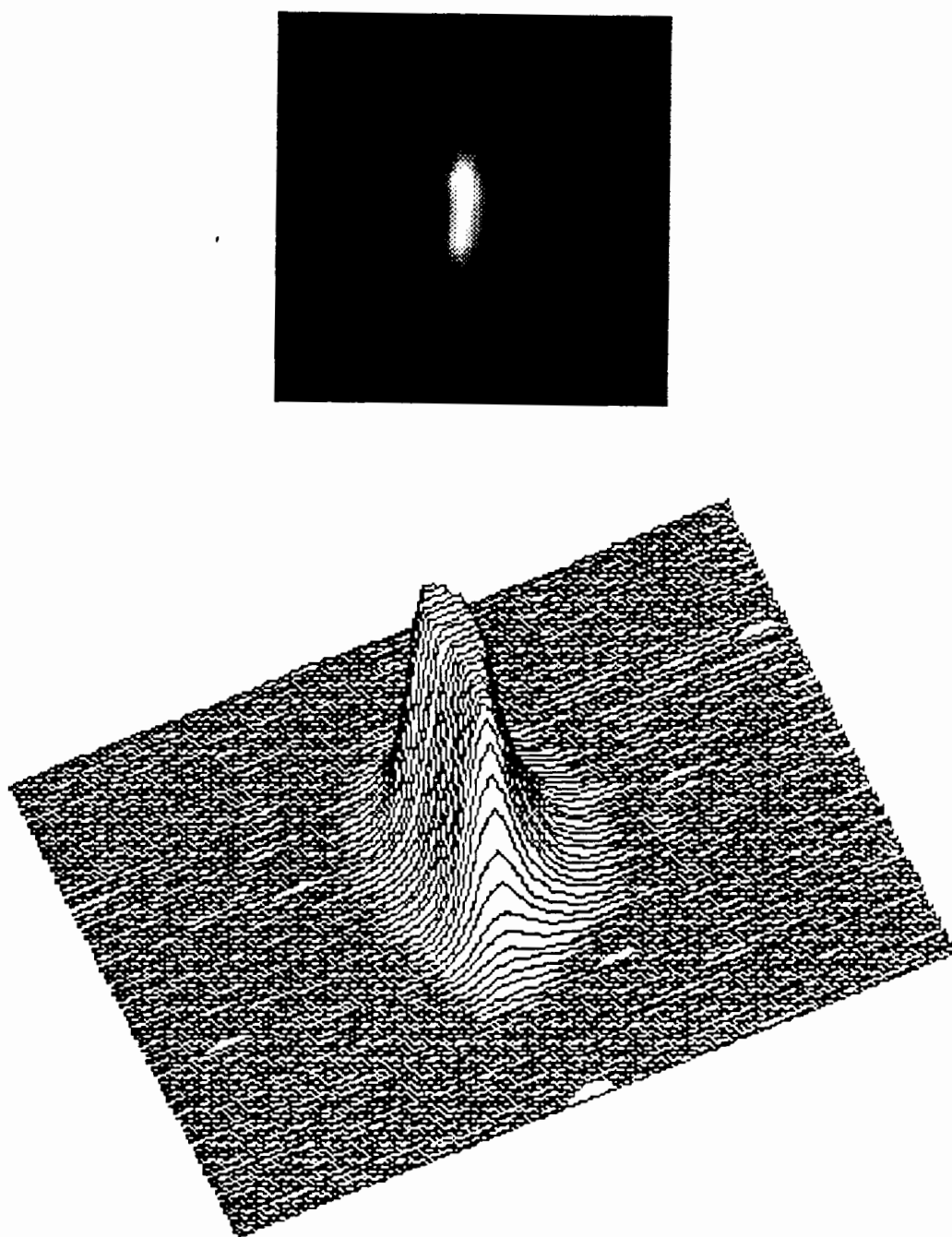


Figure 29: Beam spot OTR pattern from front surfaced mirror in the primary chamber and associated three dimensional plot. Beam energy 96 MeV.

images. The reoccurring double peaked intensity of the beam spot is also easily identified in the three dimensional plot of Figure 28. For all three of these targets in the primary chamber, attempts at focusing and steering the electron beam to obtain a circular beam spot image were ineffective. Despite this, extensive analysis of additional captured OTR images proved worthy.

Since the target ladder moves vertically in a plane, all targets will see the same beam cross-sectional area provided beam focusing is not changed while raising or lowering the ladder. A mechanism therefore exists for comparing the beam spots generated by different targets for the same beam characteristics. Since the phosphorus screen beam spots saturate at comparably lower beam currents than do the OTR images from the mirror and the gold foil, decreasing of the beam current was done frequently to prevent this saturation. Subsequently, no data was obtained for the phosphorus screen with the same beam characteristics as the gold foil and the mirror data. However, it was seen visually that the beam spot generated on the phosphorus screen was generally larger in size than the OTR images from the other two targets. The cause of this larger sized beam spot is shown in Figure 30. As the electron beam strikes the phosphorus target, the phosphorus atoms in the cross-sectional area of the beam are excited. Some secondary electrons and excited atoms excite neighboring atoms in the plane of the screen. Therefore, an enlarged beam spot is generated. Figure 31 shows this effect despite the fact that beam characteristics were not constant for all images depicted. In that figure are three electron beam spot images; one from the phosphorus screen, and two from the OTR produced on the gold foil and mirror. For the gold foil and the mirror the beam current was 0.07×10^{-8} A. The current for the phosphorus screen image was one-tenth of that value. For all images the beam energy was 96 MeV. It can easily be seen that the OTR

image from the gold foil is barely visible and that of the mirror is only slightly more intense. The phosphorus screen image however, is highly saturated. Dimensional analysis of the beam spots shows that the gold foil OTR image is approximately 0.33mm wide and 1.5mm long, the mirror OTR image is approximately 0.61mm wide and 1.5mm long, and the phosphorus screen image is approximately 0.94mm wide and 2.05mm long. It is therefore believed that the OTR images produced represent a truer electron beam spot size than the phosphorus screen images.

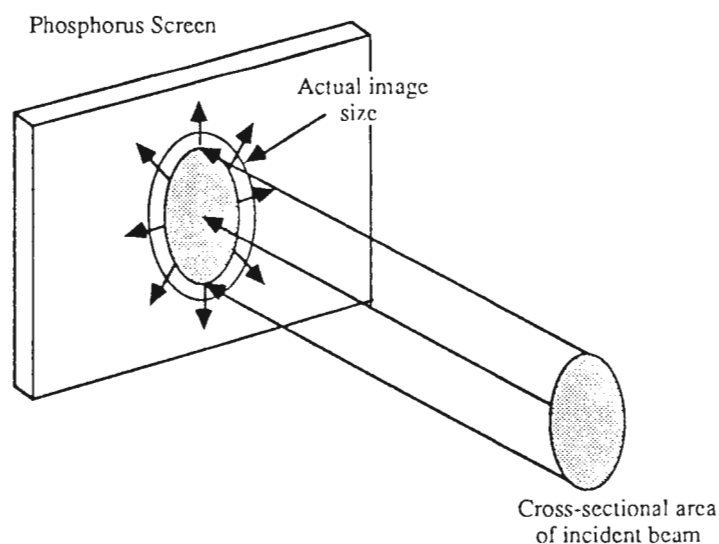
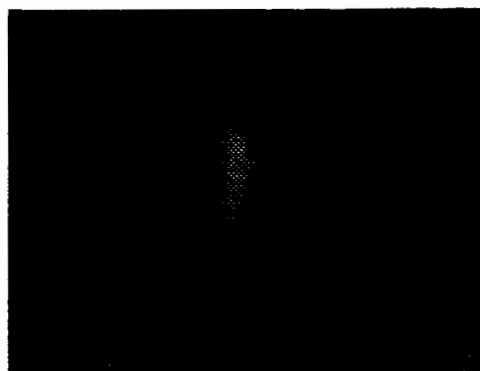


Figure 30: Expansion of the electron beam spot generated on a phosphorus screen.

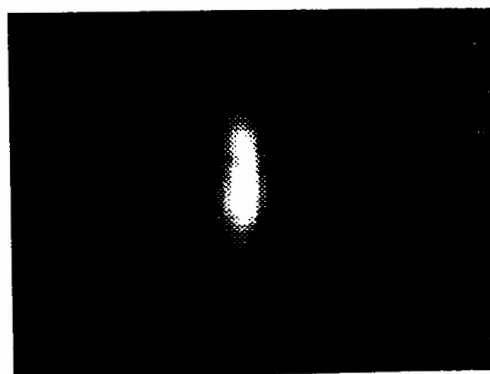
Although no present application is seen for this data, Figure 32 shows the beam spot OTR pattern as generated by the aluminum frame of the target ladder. Figure 33 shows a split image OTR pattern that was generated when the electron beam actually struck the ladder frame and the mirror at the same time. Since the frame and the mirror are not in the same vertical plane, the OTR is seen from slightly different angles, and hence a split image is formed.



Gold foil: beam spot 0.33×1.5 mm, SEM current 0.07×10^{-8} A.



Front surfaced mirror: beam spot 0.61×1.5 mm, SEM current 0.07×10^{-8} A.



Phosphorus screen: beam spot 0.94×2.05 mm, SEM current 0.07×10^{-9} A.

Figure 31: Comparison of the size of beam spots generated for different targets with the same beam focusing. Beam energy 96 MeV, Beam currents as shown.

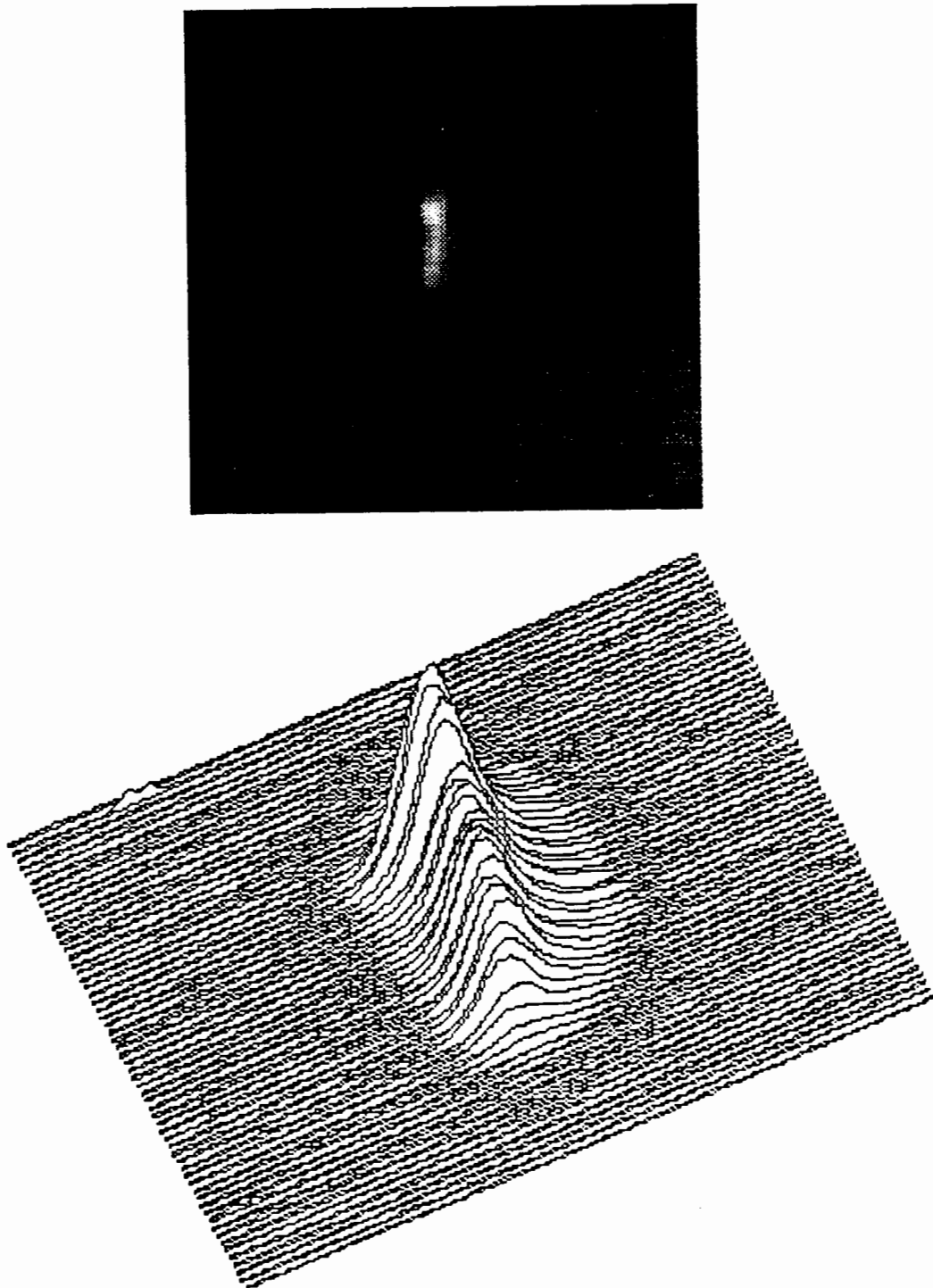


Figure 32: OTR beam spot generated from the aluminum frame of the target ladder and associated three dimensional plot. Beam energy 96 MeV.

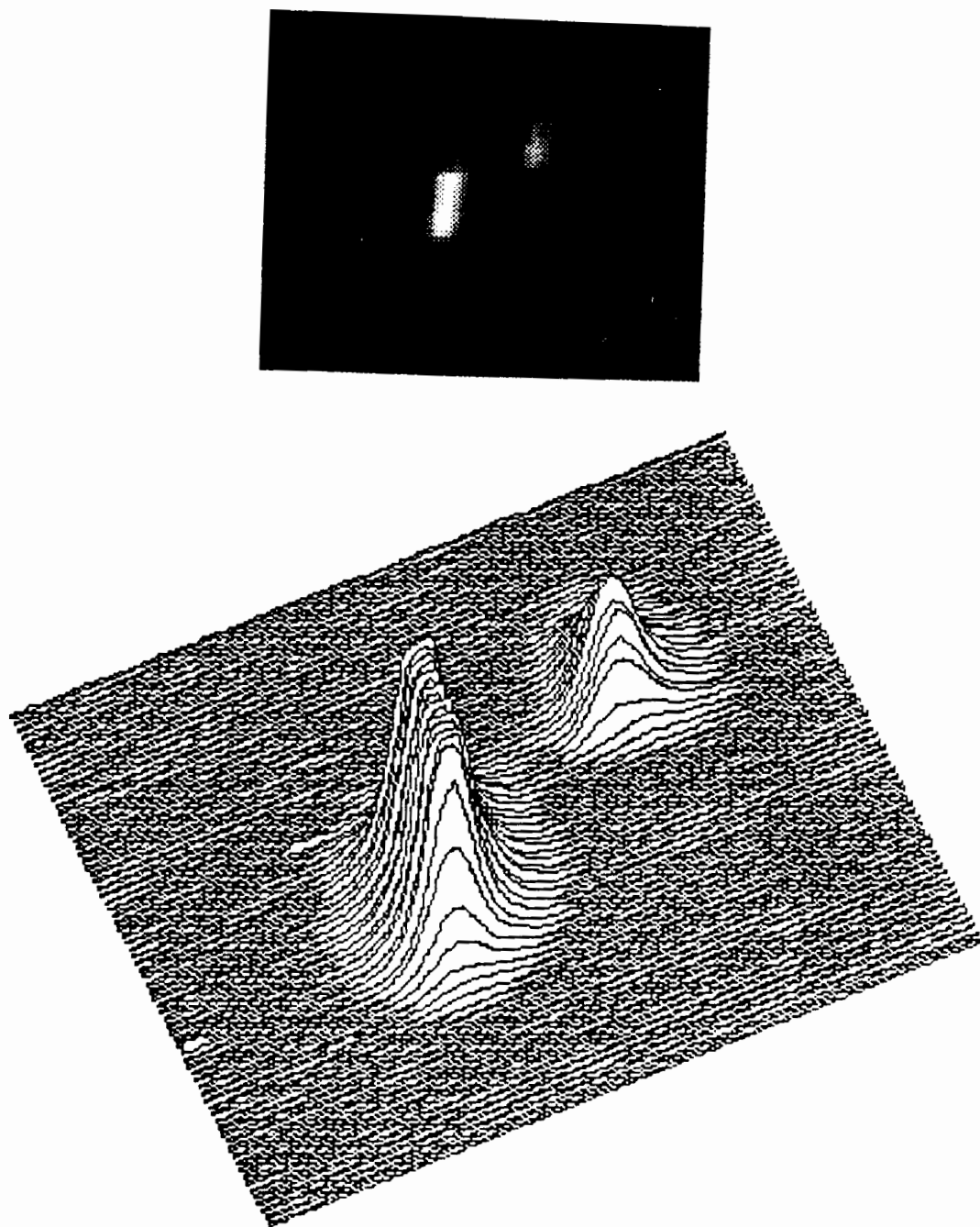


Figure 33: Split image OTR beam spot generated when the electron beam struck the target ladder frame and the mirror at the same time. Image is split due to the fact that the mirror and the frame are not in the same vertical plane, and therefore the OTR is radiated from slightly different angles.

As in the case of the OTR foil, a series of beam spot OTR images were captured from the gold foil and the mirror for a variety of beam currents. The integrated density function was then used to evaluate the OTR signals. The same procedure of recording nominal intensities of 100%, 90%, 50%, and 10% of maximum intensity was also repeated. The results for the gold foil images are shown in Figures 34 and 35 while those for the mirror are shown in Figures 36 and 37. As can be seen, all plots show a linear relationship. For similar lines in each plot however, the slopes are not the same. For example, note that the mirror saturates more rapidly than does the gold foil. A comparison of these results with those from the OTR foil shows that the OTR foil saturation point is somewhere in between that of the gold foil and the mirror. The most important piece of information that one can gather from the data is that the calculation of beam current based on captured beam spot OTR images appears to be effective for a variety of targets, and that the intensity of the generated OTR is linearly proportional to the beam current.

Since cameras were set up at positions #2 and #3, it was possible to verify the angular dependence of the beam spot OTR pattern. In order to do this, the phosphorus screen was placed perpendicularly in the line of the electron beam. With the camera at position #2 the glow of the screen was immediately visible. The ladder was then rotated clockwise so that the glow was visible with the COHU at position #3 at the same time. The target ladder was then placed in its original position and the mirror was placed in the line of the electron beam. No OTR was seen with either camera at this point. The ladder was again rotated clockwise only this time in small increments, until a beam spot OTR image appeared at position #2. The rotation was continued until the OTR pattern disappeared from position #2 and reappeared in position #3. This procedure verified the angular dependence of the beam spot OTR pattern and

SIGNAL INTEGRATED DENSITY VERSUS
SEM CURRENT FOR BEAM SPOT OTR IMAGES
FROM GOLD FOIL

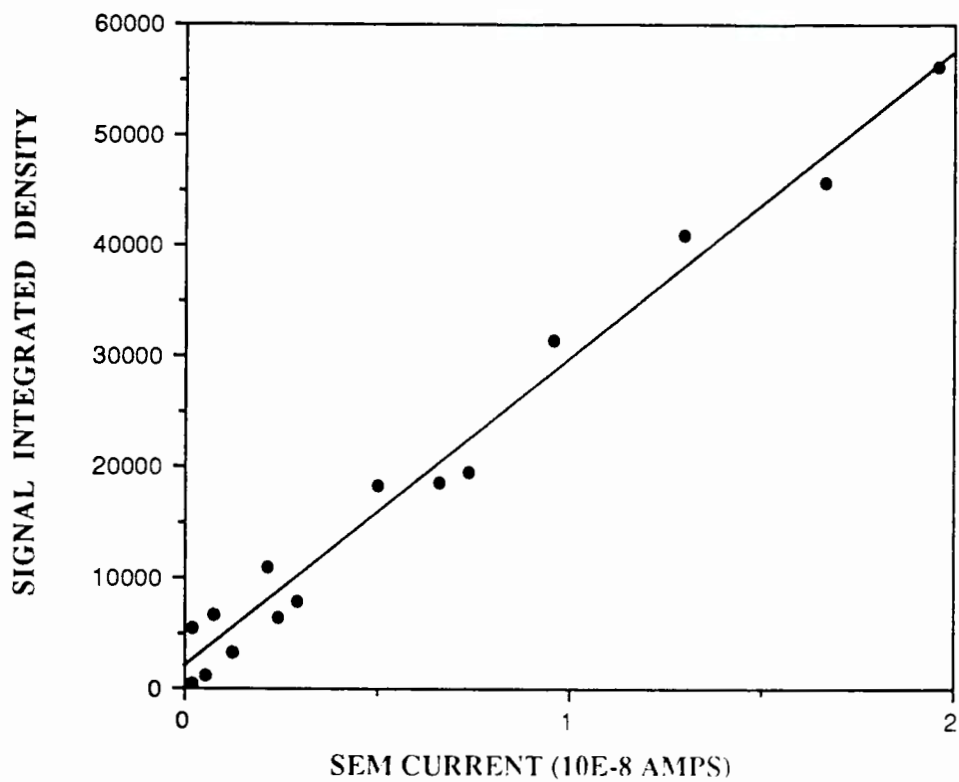


Figure 34: Plot of signal integrated density versus SEM current for beam spot OTR images from the gold foil. Beam energy 96 MeV.

**PIXEL INTENSITY VERSUS SEM CURRENT
FOR BEAM SPOT OTR IMAGES
FROM GOLD FOIL**

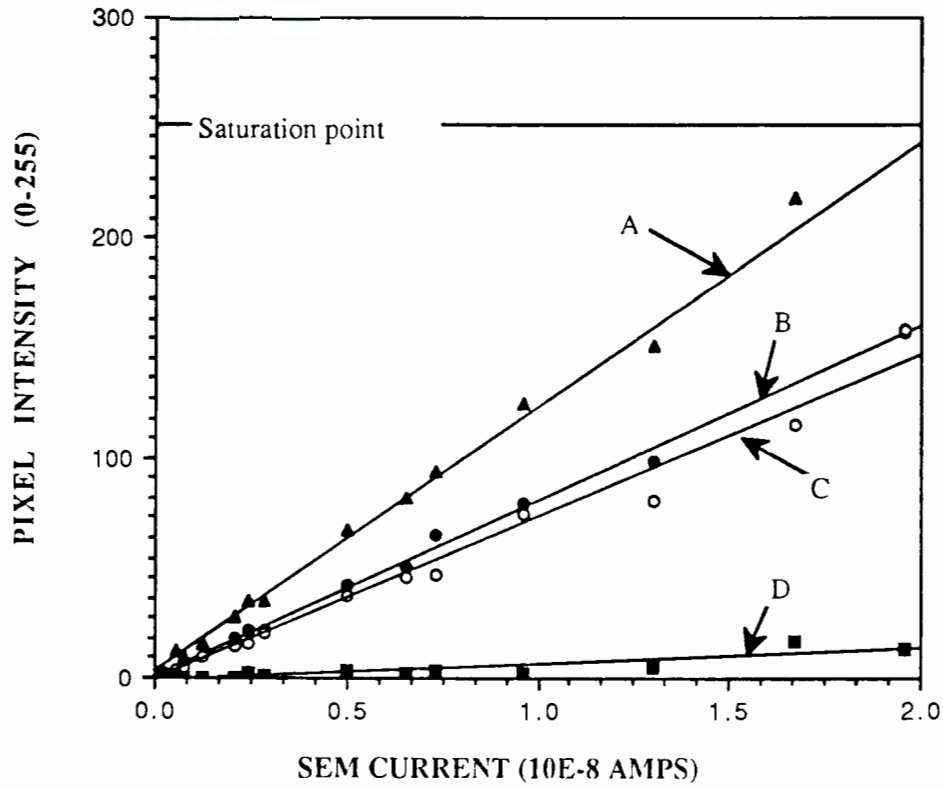


Figure 35: Pixel intensity as a function of SEM current for beam spot OTR images from gold foil. Pixel locations are fixed and are referenced as a percentage of the maximum intensity of the beam spot generated at the highest beam current. A - 100%, B - 66%, C - 60%, D - 6% of maximum intensity. Beam energy 96 MeV.

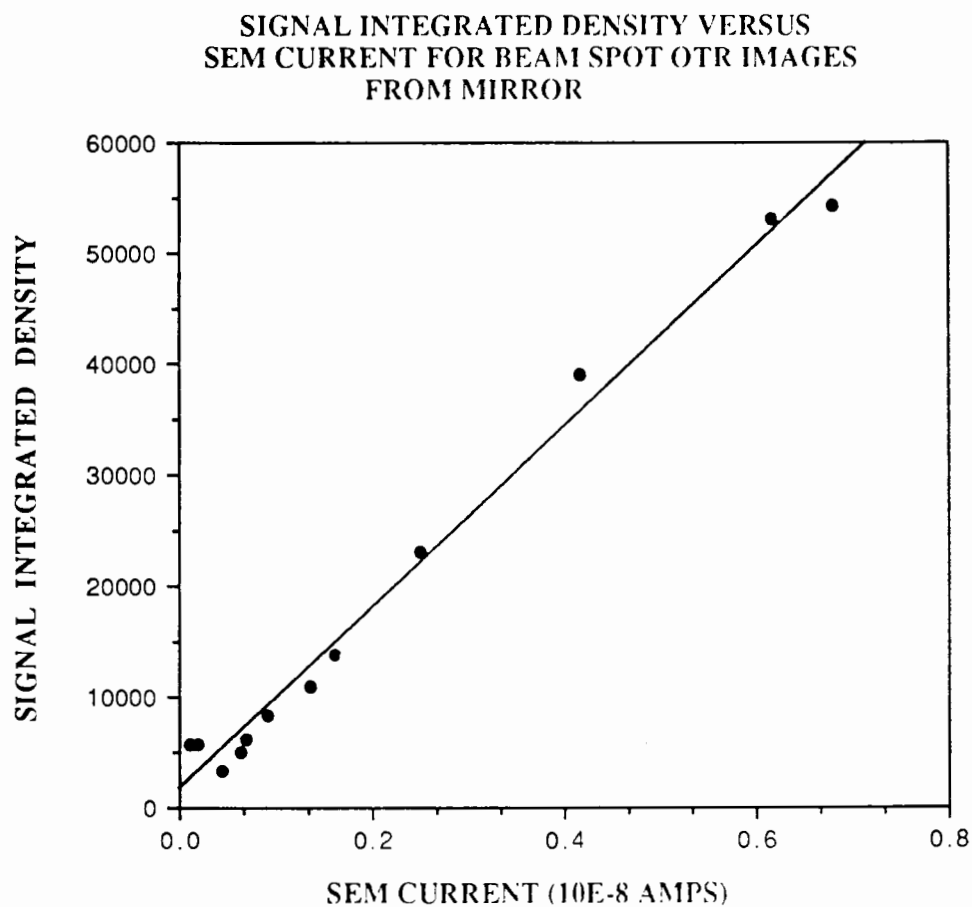


Figure 36: Plot of the signal integrated density versus SEM current for beam spot OTR images from the front surfaced mirror. Beam energy 96 MeV.

PIXEL INTENSITY VERSUS SEM CURRENT
FOR BEAM SPOT OTR IMAGES
FROM FRONT SURFACED MIRROR

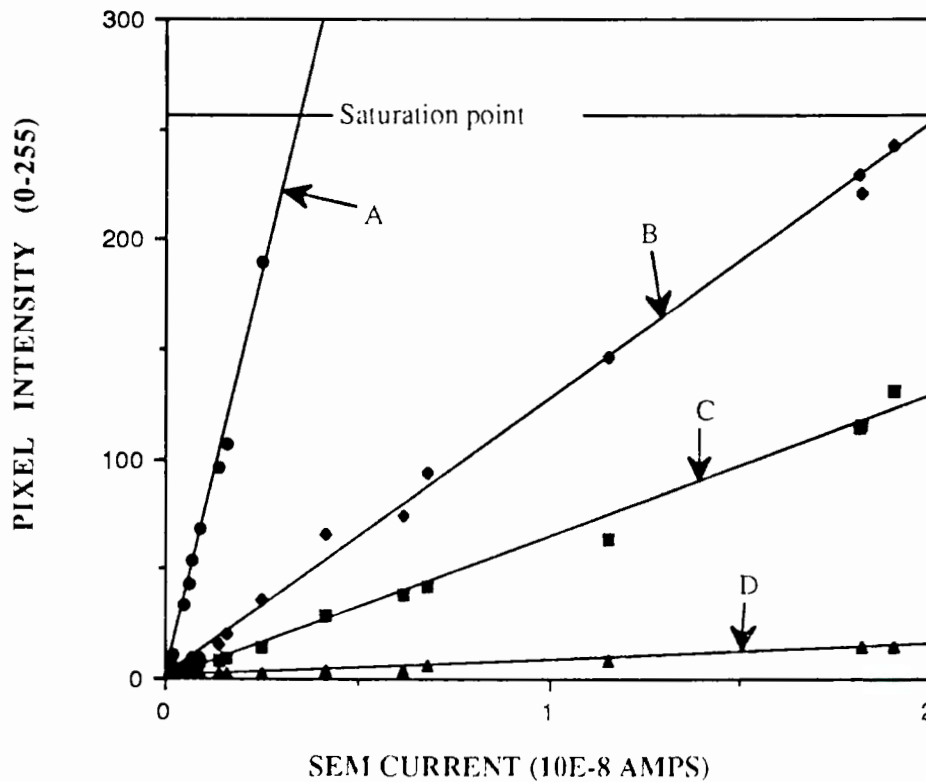


Figure 37: Pixel intensity as a function of SEM current for beam spot OTR images from the front surfaced mirror. Pixel locations are fixed and are referenced as a percentage of the maximum intensity of the beam spot generated at the highest beam current. A - 100%, B - 17%, C - 9%, D - 3% of maximum intensity. Beam energy 96 MeV.

insured that the images captured were not simply the phosphorescence of the various targets.

The last procedure to be undertaken was to attempt to see the radiation cone OTR pattern. The 200 mm lens was translated to the point where the COHU was placed in the focal plane of the lens. No radiation cone OTR was seen however. Recall from the optical ray diagram of Figure 5 that this pattern involves the radiation that comes off parallel from the target surface. Since no system was available for focusing the electron beam at infinity, it was determined that the focusing magnets should be adjusted until the best possible radiation cone OTR pattern was obtained. After several attempts, an extremely faint image appeared on the computer screen. The output from the COHU was then placed into a high resolution video monitor, and the radiation cone OTR pattern was seen. Figure 38 shows a polaroid snapshot of the monitor screen. Although the image is cluttered with interference, the expected donut shaped pattern is clearly visible. Not only was the beam focusing changed to allow for viewing the radiation cone OTR pattern, but the beam current used was ten times that used for capturing the beam spot OTR images. It was determined that the interference in the image was caused by the increased radiation as a result of the excessive beam current. As the beam current was decreased, not only did the interference disappear, but the intensity of the OTR image also decreased drastically. The image shown in Figure 38 was determined to be the best one obtained for the various adjustments in beam current and focusing. The output from the COHU was then placed in the computer, and an image was captured. Again, the image that was displayed on the computer screen was very faint. However, with the assistance of a software option that allows for viewing images in false color, the radiation cone OTR pattern was seen on a

captured image. Figure 39 shows a black and white print of that image along with a horizontal two dimensional line intensity scan through the image. The intensity scan shows clearly the expected double hump but more importantly, it shows that the intensity of the image is only slightly above that of the background. One can therefore gain some understanding of the need for sensitive video capturing devices in OTR experiments.

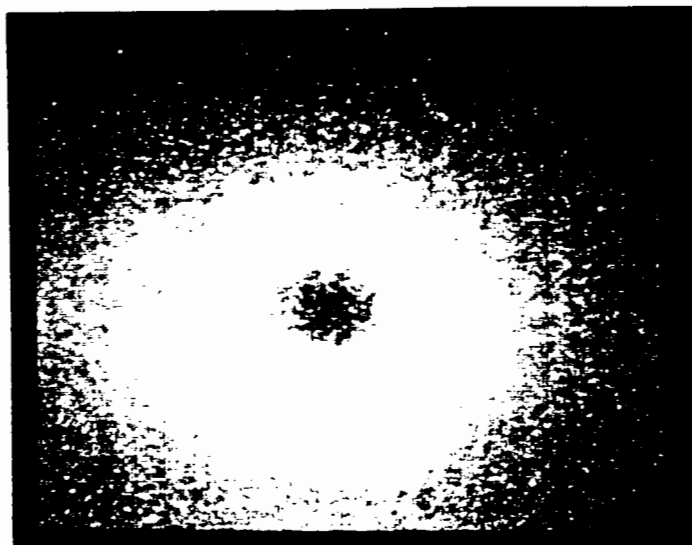


Figure 38: Polaroid snapshot of the radiation cone OTR pattern as seen on a video monitor, Beam energy 96 MeV, SEM current 11.1×10^{-8} A.

With a captured radiation cone OTR pattern, a calculation of γ , the Lorentz factor is possible. Recall from Figure 2 that the peak intensity of the radiation cone OTR occurs at the angle $\theta = 1/\gamma$. Therefore, a calculation of the angle at peak intensity is required. Figure 40 shows the geometry behind this calculation. Since the camera is in the focal plane of the lens, only parallel rays incident to the lens will be focused there. Geometric optics proves that those parallel rays are focused to the same spot in the focal plane. It also proves that any ray passing through the center of the lens is undeviated in its path. Two of the most intense rays are drawn in Figure 40. Note that both of

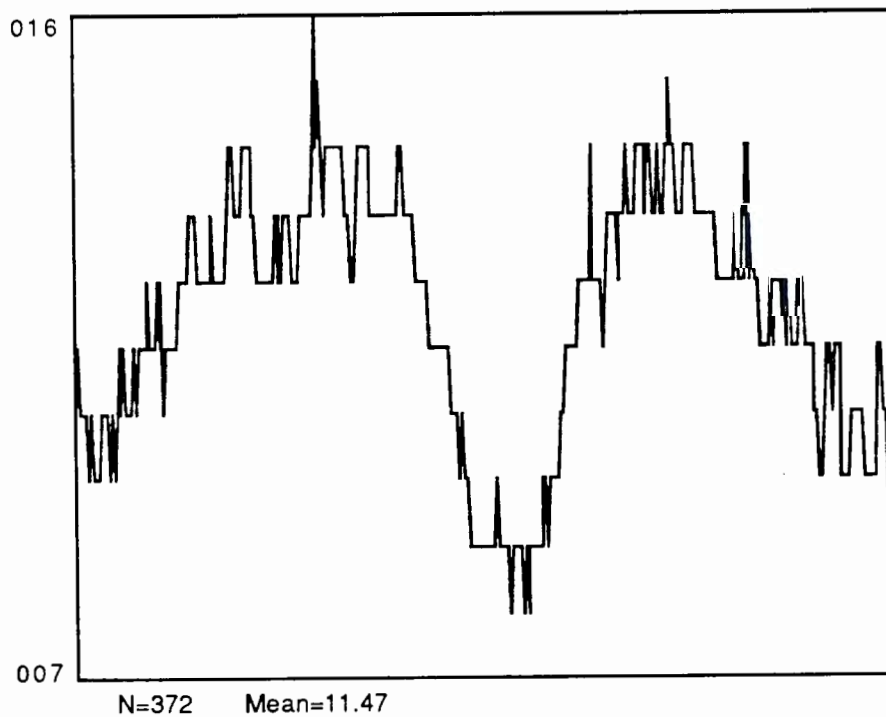
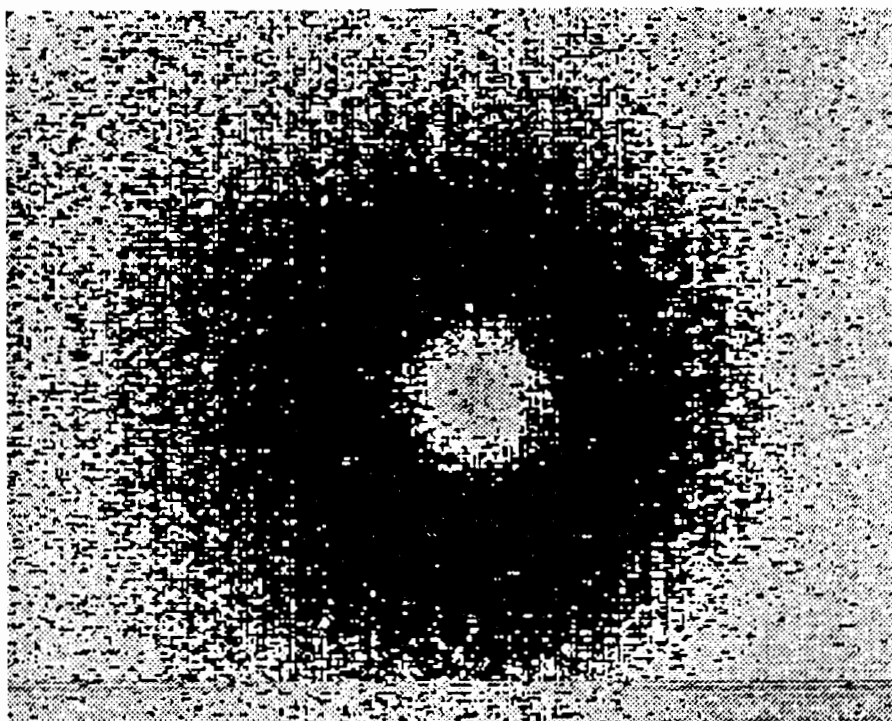


Figure 39: Black and white print of the captured radiation cone OTR pattern from the front surfaced mirror and associated line intensity scan. Beam energy 96 MeV, SEM current 11.1×10^{-8} A.

them leave the OTR foil at an angle θ with respect to the normal. One of the rays is drawn through the center of the lens, and therefore leaves the lens at the same angle θ with respect to the perpendicular centerline of the lens. It is easily verified that $\theta = \tan^{-1} d/f$ where d is the distance from the center of the radiation cone to the point of maximum intensity, and f is the focal length of the lens, 200 mm.

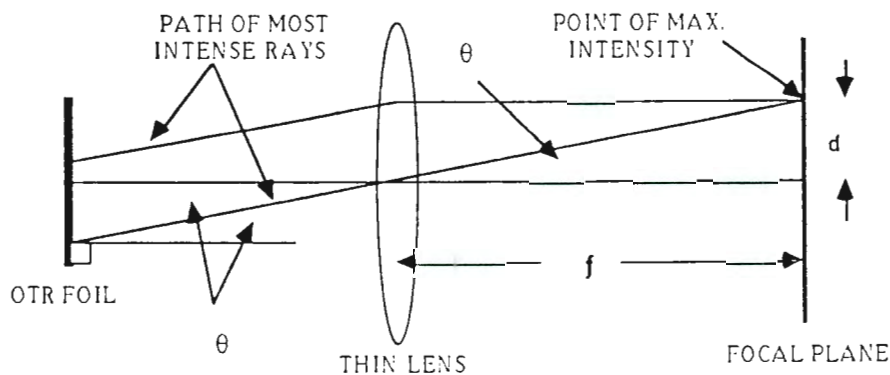


Figure 40: Optical geometry used in calculating γ , the Lorentz factor.

Since the focal length of the lens is known, the distance d must be calculated. Recall from earlier discussion, that dimensional calibration was done for images captured while the 200 mm lens was focused to see beam spot OTR. A separate calibration was required for the lens focused to see radiation cone OTR. To accomplish this a 3 mm wide object was affixed to the sector star focusing device. Figure 41 shows an actual sector star image as captured when the lens was focused at infinity. Once this calibration was accomplished, the distance d from above could be obtained directly from the radiation cone OTR pattern. For the captured OTR image, the distance d was measured to be approximately 1.82 mm which corresponds to a Lorentz factor of 110. The

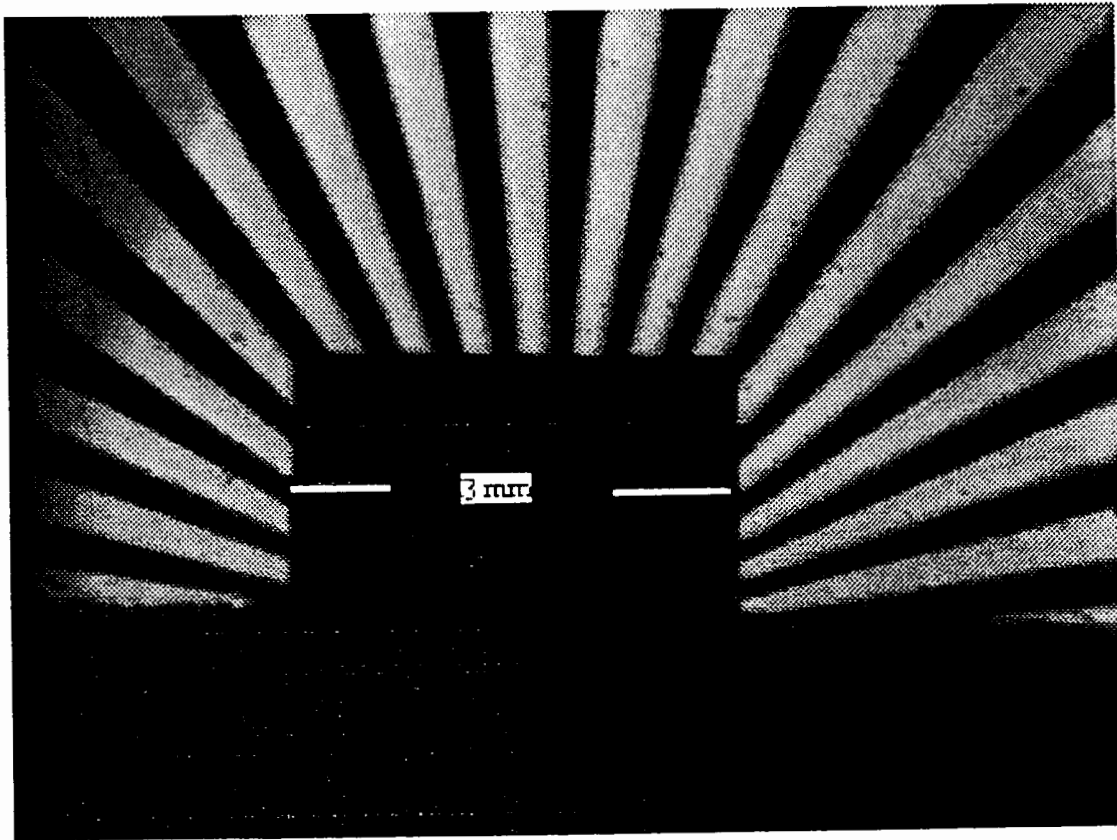


Figure 41: Captured image of the sector star mechanism used for focusing at infinity and calibrating the computer screen to dimensionally known lengths.

Lorentz factor as computed from beam energy was 187. The large discrepancy of the experimentally calculated value may possibly be attributed to two things. Firstly, as was mentioned above, it was uncertain whether or not the electron beam had minimum angular divergence and since the quality of the beam was already shown to be poor, the focusing could be ineffective. Secondly, since the radiation cone pattern for this experiment was approximately 15 times the size of the beam spot pattern, the intensity of the radiation is spread over a larger area resulting in a lower intensity per pixel. The low intensity and the background makes the determination of the radiation profile difficult and may cause an inaccurate measurement of the distance d .

B. CONCLUSIONS

It has been shown that the experimental technique and the equipment used provide an effective means of observing and analyzing captured OTR images. The setup is easily established, and is readily maintained during the experiment. Once accomplished, the extensive alignment procedure allows for relocation of image gathering cameras to enable experimenters to gain a fuller understanding of the processes at hand. The COHU camera with an experimentally determined accuracy of 0.6 % at high intensity regions and 15% at lower intensity regions, was shown to be superior in performance to the RCA Vidicon used in previous experiments. This superior performance allowed for extensive analysis of the captured beam spot OTR patterns, and visualization of the radiation cone OTR pattern.

The *Image* software was used extensively throughout the experiment, and was proven to be a vital part of the setup. It not only provided the means by which OTR images were captured, but it also allowed for detailed analysis of the data. Of the software options discussed, the Integrated Density function and the three dimensional plot option proved to be the most beneficial in providing as much information as possible on OTR patterns. When integrated densities of electron beam spot OTR images were plotted as a function of the SEM current, a distinct linear relationship was seen. This was shown for three different targets; the OTR foil, the gold foil, and the front surfaced mirror. Therefore a means of computing electron beam current from captured beam spot OTR images was developed. Two methods were used to evaluate the background or noise level within the captured beam spot OTR images. Both methods proved that the background was not constant, and that variations of as much as three times the average were obtained. A technique was adopted for plotting the beam spot intensity as a function of the beam current over the entire

intensity spectrum. For intensity values of 100%, 90%, 50% and 10% of the maximum intensity of the beam spot at the highest beam current, more linear relationships for all three targets were shown. The similar plots for each target did not show the same linear dependence however, as the front surfaced mirror saturated more rapidly than the other two targets, and the gold foil saturated slowest of all. The gold foil was not a polished mirror surface. Despite this, it was shown that the intensity of the beam spot OTR image is proportional to the beam current for a variety of target devices. The three dimensional plots of several images showed the assymetric intensity distribution of the electron beam. These same plots showed the unexpected double intensity peak.

It was seen that despite all efforts, the beam spot OTR pattern could not be focused into a circle. This was true for all three OTR targets used as well as for the phosphorus screen. The best focusing created an elliptical beam spot that was elongated in the vertical direction. Four separate images were captured for what were considered constant beam parameters. Comparison of those images showed that the beam spot varied extensively in internal structure as well as in intensity. This result along with the information provided by the three dimensional intensity plots showed that the quality of the electron beam was not ideal.

Dimensional analysis was performed on the beam spots generated on the phosphorus screen, the gold foil, and the front surfaced mirror. It was shown that the phosphorus screen images saturated rapidly for even the lowest beam currents, and that the size of beam spots on the gold foil and mirror were smaller than those on the phosphorus screen even when there existed a magnitude of ten difference in beam current. It is believed that the image

shown on the phosphorus screen does not represent a true beam profile, since excitation of neighboring atoms on the screen occurs and enlarges the image.

Finally, a radiation cone OTR pattern was captured by excessively increasing the beam current, and altering the focusing magnets. The resulting image showed extensive interference that was proven to be caused by the increased radiation from the higher currents. A two dimensional intensity scan through the image showed clearly the expected double hump, and also verified the low strength of the captured signal. A calculation of the Lorentz factor was performed based on the OTR pattern, and a comparison with the actual value showed a large variation. This large variation is believed to be from the poor quality of the captured OTR image, the limitations of the camera and the software, and the uncertain focusing of the electron beam. This observation of the OTR image from the beam profile shows the utility as a beam diagnostic.

C. RECOMMENDATIONS

Recommendations for continued work in this area include:

1. Placing a second focusing device in the secondary chamber to allow for a more thorough coupling of the laser beam and the electron beam paths. This device must be removable so that the OTR foil or similar target may be placed in the line of the beam. An arm similar to that in the primary chamber is recommended.
2. Although not previously mentioned, a technique for aligning the laser beam while the system is under vacuum would prevent the frequent opening of target chambers. Often after the chambers were opened, it was difficult to quickly reestablish vacuum.

3. A technique for creating a parallel electron beam is required. If this can successfully be done, a finer quality radiation cone OTR image may be seen, and a more accurate calculation of the Lorentz factor may be done.
4. Provided recommendation #3 is met, it may be proven that the COHU camera is not sensitive enough to distinguish the signal from the background while focused for radiation cone OTR patterns. A more sensitive camera may be required.
5. Depending on the camera used, some shielding from radiation effects may be necessary.
6. Further investigation is required into the cause of the non-circular shape of the beam spot OTR pattern. This may help eliminate the unexpected double peak intensity. This recommendation pertains to the accelerator system characteristics, not to the OTR imaging.

APPENDIX A. LIST OF EQUIPMENT

MANUFACTURER

PART NUMBER ; NAME ; PURPOSE

Newport

LS-35 ; optical bench ; mounting components on.

U-1301 ; class IIIA 1 milliwatt Helium-Neon laser ; aligning purposes.

812 ; laser mount ; two degrees of freedom for laser alignment.

MRL-3 ; micro optical rail ; securing optical components to.

280 ; lab jack ; securing components to for 3" to 6" height control.

270 ; lab jack ; securing components to for 2" to 4" height control.

B-1 and B-2 ; sliding base ; slides along optical rail for continued alignment.

20Z20BD.1 ; 20th wave zerodur mirror ; reflects laser light.

MT-X ; microtranslator stage ; 1/4" travel stage.

ID-1.0 ; iris diaphragm ; aperture to control incoming light.

CLMK-B2 ; lens holder ; holds 200 mm Canon lens.

Canon

200 mm/1:2.8 ; Camera lens ; focuses OTR light.

Oriel Corporation

11512 ; optical rail ; 24" x 4" rail for mounting optical components.

11522 ; standard rail ; 24" x 2" ; rail for mounting laser beam components.

40780 ; plano-convex lens ; 2" diameter lens with $f = 200$ mm, infinity focus.

50350 through 50390 ; neutral density filters ; reduces light intensity.

18011 ; Encoder Mike Controller ; digitally controls motorized stages.

16338 ; 2" motorized translation stage ; translates 200 mm Canon lens.

Ealing Electro-Optics, Inc.

2668P74 ; sector star ; focussing device.

228437 ; electronic shutter ; protects optical devices from intense light.

Process Physics, Inc.

C6C-0800 ; six-way vacuum chamber ; acts as secondary chamber.

COHU

4815-5000 ; solid state CCD camera ; allows for observation of OTR.

Huntington Mechanical Laboratories, Inc.

VF-156 ; 2" translational arm ; 45° alignment arm.

RCA

TC2011 ; solid state CCD camera ; allows for viewing OTR.

Panasonic

TR-930U ; video monitor ; allows for viewing beam spot on phosphorus screen.

LIST OF REFERENCES

1. Frank, I., and Ginsburg, V., "Radiation of a Uniformly Moving Electron Due to It's Transition From One Medium Into Another," Journal of Physics, Vol. IX, No. 5, pp. 353-362, 1945.
2. Naval Surface Weapons Center Report TR 84-134, "The Use of Transition Radiation as a Diagnostic for Intense Beams," by Dr. D.W. Rule and Dr. R.B. Fiorito, July, 1984.
3. Ginzburg, V., and Tsytovich, V.N., "Several Problems of the Theory of Transition Radiation and Transition Scattering," Physics Reports, Vol. 49, No. 1, p. 6, 1979.
4. Ginzburg, V., "Transition Radiation and Transition Scattering," Physics Scripta, ol. T2/1, p. 182, 1982.
5. Maruyama, X.K., Fiorito, R.B., and Rule, D.W., "Optical Transition Radiation as a Real-Time, On-Line Diagnostic for Free Electron Laser Systems," Nuclear Instruments and Methods in Physics Research, A272, 1988.
6. Private communication between Dr. Donald Rule, Naval Surface Warfare Center, and the author, September 1989.
7. Wartski, L., *Study on the Optical Transition Radiation Produced by 30 and 70 Mev Energy Electrons. Application to the Diagnosis of Charged Particles*, Ph. D. Dissertation, The Universite de Paris-Sud, Centre D'Orsay, France, 1976.
8. Longstaff, W.G., *Three Dimensional Analysis of Optical Transition Radiation*, Master's Thesis, Naval Postgraduate School, Monterey, California, December 1988.
9. Dallman, P., *Establishment of a Capability to Measure Optical Transition Radiation*, Master's Thesis, Naval Postgraduate School, Monterey, California, December 1989.
10. Private communication between Dr. X.K. Maruyama, Naval Postgraduate School, Wayne Rasband, National Institutes of Health, Research Services Branch, and the author, January 1990.

INITIAL DISTRIBUTION LIST

	No. Copies
1. Defense Technical Information Center Cameron Station Alexandria, VA 22304-6145	2
2. Library, Code 0142 Naval Postgraduate School Monterey, CA 93943-5002	2
3. Physics Library, Code 61 Department of Physics Naval Postgraduate School Monterey, CA 93940-5100	1
4. Professor X.K. Maruyama, Code 61Mx Department of Physics Naval Postgraduate School Monterey, CA 93943-5002	6
5. Professor J.R. Neighbours, Code 61 Nb Department of Physics Naval Postgraduate School Monterey, CA 93943-5002	1
6. Professor F. Buskirk, Code 61 Bs Department of Physics Naval Postgraduate School Monterey, CA 93940-5002	1
7. Dr. D.W. Rule, Code R41 Naval Surface Warfare Center Silver Spring, MD 20903-5000	1
8. Dr. R.B. Fiorito, Code R41 Naval Surface Warfare Center Silver Spring, MD 20903-5001	1
9. Dr. M.A. Piestrup Adelphi Technology, Inc. 532 Emerson Street Palo Alto, CA 94301	1

- | | |
|--|---|
| 10. Mr. Don Snyder, Code 61Ds
Department of Physics
Naval Postgraduate School
Monterey, CA 93943-5002 | 1 |
| 11. Mr. Harold Rietdyk, Code 61Hr
Department of Physics
Naval Postgraduate School
Monterey, CA 93943-5002 | 1 |
| 12. LT. David M. Caldwell
10823 Colton Street
Fairfax, VA 22030 | 1 |
| 13. LT. Peter K. Dallman
186 Cranwood Drive
West Seneca, NY 14224 | 1 |
| 14. Dr. Richard L. Swent
W.W. Hansen Laboratory
Stanford University
Palo Alto, CA 94305 | 1 |
| 15. Dr. Douglas Beck
Department of Physics
University of Illinois, Champagne-Urbana
1110 W. Green St.
Urbana, IL 61801 | 1 |
| 16. Dr. Todd I. Smith
W.W. Hansen Laboratory
Stanford University
Palo Alto, CA 94305 | 1 |
| 17. Dr. Hartmut Backe
Institut Fuer Physik des
Universitaet, Postfach 3980
D-65 MAINZ1
Federal Republic of Germany | 1 |
| 18. Professor K.E. Woehler Code PH/Wh
Department of Physics
Naval Postgraduate School
Monterey, CA 93943-5002 | 1 |

SHOLEY KNOX LIBRARY
POSTGRADUATE SCHOOL
MONTEREY, CALIFORNIA 93943-8002

DUDLEY KNOX LIBRARY



3 2768 00003461 5